Monte Carlo based electron treatment planning and cutout output factor calculations

Ellis Mitrou

Master of Science

Medical Physics Unit

McGill University

Montreal

August 2011

A thesis submitted to the Faculty of Graduate Studies and Research of McGill University in partial fulfillment of the requirements of the degree of Master of Science

DEDICATION

This thesis is dedicated to my family: my parents, Mariella Zara and Costa Mitrou; my brothers Dean and Vince Mitrou; and my nonna Teresa Zara.

ACKNOWLEDGEMENTS

My gratitude goes to my supervisor **Dr. François DeBlois** for support and guidance throughout the project.

I am indebted to my co-supervisor, **Johnathan Thébaut** whose guidance really pushed this project forward. He made it his mission to see this project through regardless of how busy he was.

My appreciation goes to **Dr. Slobodan Devic** for advice on using GAFCHROMIC® film and troubleshooting tips. I would also like to thank him for keeping the Monday clinical meetings interesting.

Andrew Alexander was there from day one. As an undergrad I worked with Andrew on MMCTP, he helped guide me through the then unknown world of medical physics. For this project, Andrew played a crucial role in implementing CUTOUT into MMCTP. I am forever indebted to Andrew and view him more as an old war buddy then a colleague.

I would like to thank **Joseph Holmes** and **Marc Morcos** for important discussions and help on data analysis.

I would also like to acknowledge the support from the Segal Centre's Weekend to End Breast Cancer research fund.

ABSTRACT

Electron radiotherapy (RT) offers a number of advantages over photons. The high surface dose, combined with a rapid dose fall-off beyond the target volume presents a net increase in tumor control probability and decreases the normal tissue complication for superficial tumors. Electron treatments are normally delivered clinically without previously calculated dose distributions due to the complexity of the electron transport involved and greater error in planning accuracy. This research uses Monte Carlo (MC) methods to model clinical electron beams in order to accurately calculate electron beam dose distributions in patients as well as calculate cutout output factors, reducing the need for a clinical measurement. The present work is incorporated into a research MC calculation system: McGill Monte Carlo Treatment Planning (MMCTP) system. Measurements of PDDs, profiles and output factors in addition to 2D GAFCHROMIC® EBT2 film measurements in heterogeneous phantoms were obtained to commission the electron beam model. The use of MC for electron TP will provide more accurate treatments and yield greater knowledge of the electron dose distribution within the patient. The calculation of output factors could invoke a clinical time saving of up to 1 hour per patient.

ABRÉGÉ

La radiotherapie d'électrons offre plusieurs avantages en comparaison avec les photons. La dose de surface élevée, en combinaison avec une dose descenante plus rapide au-delà du volume prévu présente un taux plus élevé de la probabilité de contrôle tumoral et diminue les complications dans les tissus normaux en évitant les tumeurs superficiel. Les traitements d'électrons sont habituellement utilisés cliniquements sans calculations de doses prévu, due à leurs complexités du transport d'electron qui sont impliqués et plusieurs erreurs de precision en planification. Cette recherche utilise les methodes de Monte Carlo (MC) pour démontrer cliniquement les faisceaux d'electrons pour précisement calculer la dose d'electron distribuée au patients mais aussi pour pouvoir calculer les facteurs de dendements de cutout, et ceci réduit le besoin d'une mesure clinique. Ce projet a été élaboré dans un environnement de calculation par MC: McGill Monte Carlo Treatment Planning (MMCTP) System. Mesure de pourcentage de dose en profondeur, profiles et les facteurs de rendements de cutout ainsi que de doses mesurés avec des films GAFCHROMIC® EBT2 dans les phantoms hétérogène ont été obtenu pour déléguer la modèle de faisceau d'electron. L'utilisation de MC pour l'électrode TP sera apporter des traitements plus précis et en consequence produire plus de connaisance de la dose d'electrons plus approprié pour le patient. Ces attributions pourront sauver jusqu'à une heure par patient en terme de temps passé en clinique.

TABLE OF CONTENTS

LIST OF TABLES

LIST OF FIGURES

CHAPTER 1
Introduction to Electron Beam Radiotherapy

Contents

1.1 Aspects of Electron Beams

Electron beams provide an important treatment modality in radiotherapy for the treatment of superficial tumors. This is due to the nature of the electron beam's central axis depth dose curve in water.

To graphically represent the depth dose of a clinical beam, we must look at a function called the percentage depth dose (PDD). The PDD of a beam is the ratio of the dose in water at a given depth to the maximum dose along the central axis of the beam, as seen in equation 1.1.

$$\mathrm{PDD}(z, A, f, E) = \frac{D(z, A, f, E)}{D(z_{\max}, A, f, E)} \times 100 \tag{1.1}$$

Where z is the depth in water, $z_{\max}$ is the depth of maximum dose, A is the field size, defined at the surface of the phantom, f is the source to surface distance (SSD) and E is the nominal energy of the beam. The geometry of the PDD measurement is shown in figure 1–1.

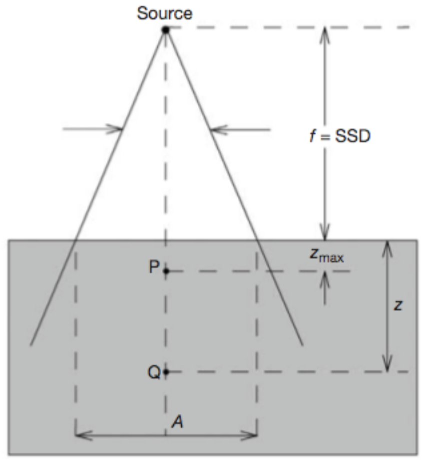

Figure 1–1: Geometry of the PDD measurement for a clinical radiotherapy beam. Reproduced from E.B. Podgorsak, Radiation Oncology Physics: A Handbook for Students and Teachers, page 180 [8]

As opposed to photon beams, electron beams offer a relatively high surface dose with a steep falloff within the medium. For this reason, electron beams are a good candidate for the treatment of superficial tumors, at a depth of up to about 5 cm. The PDD of a typical electron beam is shown in figure 1–2, and a family of PDD curves for various energies for typical electron beams is shown in figure 1–3

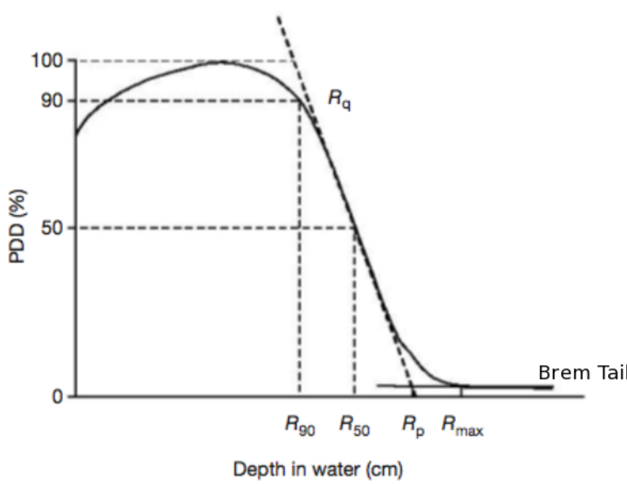

Figure 1–2: Typical electron beam PDD with various depth definitions shown. Reproduced from E.B. Podgorsak, Radiation Oncology Physics: A Handbook for Students and Teachers, page 278 [8].

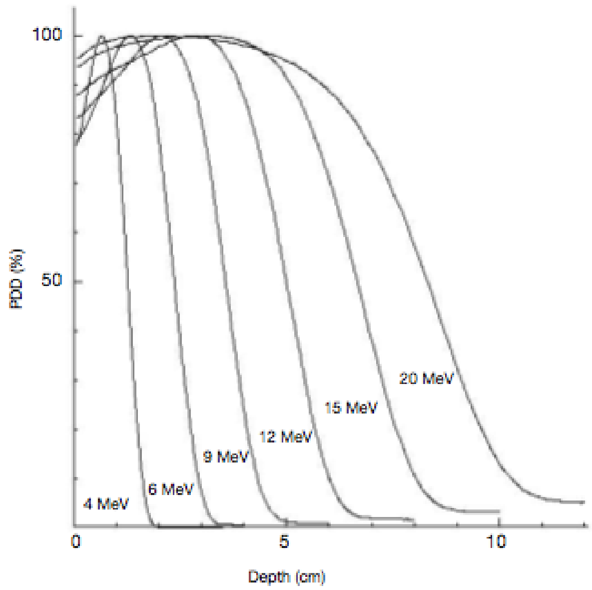

Figure 1–3: Typical electron beam PDDs for various electron energies. Reproduced from E.B. Podgorsak, Radiation Oncology Physics: A Handbook for Students and Teachers, page 280 [8].

The major aspects of the PDD curve are a high surface dose followed by a buildup region to a maximum dose. After the maximum dose there is a steep dose falloff and finally a bremsstrahlung tail. The distributions in figures 1–2 and 1–3 are for normal beam incidence on the phantom. When obliquity in the angle of incidence is introduced, there is a significant change in the PDD for angle of incidence, α between the beam central axis and normal to the phantom surface [8]. Figure 1–4 depicts the effect of oblique angle of incidence for electron beams.

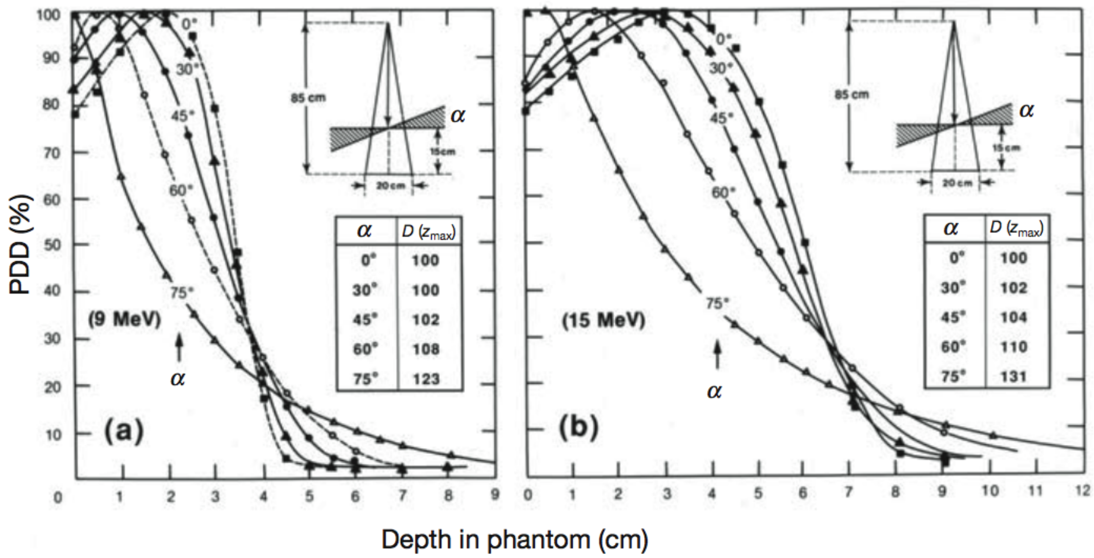

Figure 1–4: PDD curves for various beam incidences for two beam energies. 9 MeV in (a) and 15 MeV in (b). The geometry of the experimental setup is shown in the insert in the top-right corner of each figure. Reproduced from E.B. Podgorsak, Radiation Oncology Physics: A Handbook for Students and Teachers, page 284 [8].

The angle $\alpha = 0^0$ is for normal incidence and the larger the angle α, the shallower is the depth of maximum dose , $z_{\max}$ and the greater is the dose at $z_{\max}$.

As visualized in figure 1–2, the parameters R_{50} and R_{90} represent the depth at which the dose falls off to 50% and 90% respectively. R_{p} is the practical range of the beam and is defined as the the depth in water at which the tangent of the inflection point of the curve intersects the tail of the PDD curve, caused by bremsstrahlung contamination. $R_{\max}$ is the depth at which the PDD curve intersects the flat portion of the bremsstrahlung tail [8]. Electrons may interact thousands of times before depositing all of their energy within a medium, so to simplify matters, physicists usually approximate the dose deposition with what is known as the continuous slowing down approximation (CSDA). In this approximation, the kinetic energy of the electron is assumed to be continuously lost to the medium and a CSDA range, R_{CSDA} can be defined as follows:

$$R_{\mathrm{CSDA}} = \int_0^{E_{K_0}} \frac{dE}{S_{\mathrm{tot}}(E)} \tag{1.2}$$

Where R_{CSDA} is the CSDA range of the charged particle in the absorber, E_{K_0} is the initial kinetic energy of the electron and $S_{\mathrm{tot}}(E)$ is the stopping power of the electron as a function of kinetic energy. Stopping power is described in section 1.2. For heavy charged particles, R_{CSDA} is a good approximation to the average range of the particles within the medium because of the virtually linear path of the particles in the absorber. For light charged particles on the other hand, R_{CSDA} can be up to twice as large as the actual range of the particles because of the very tortuous path the particles undergo in the absorber [9].

1.2 Interactions of Electrons with Matter

As charged particles, such as electrons travel through a medium, several different interactions can occur in succession. A charged particle has an electric field surrounding it and this field will interact with the orbital electrons and the nucleus of the atoms of the matter it is penetrating [9]. As an electron makes its way through a material, it gradually loses energy by undergoing tens of thousands of interactions. The energy lost by the electron or charged particle is described by a parameter known as stopping power [9]. Stopping power is classified into two different types, *collision (ionization) stopping power* and *radiative stopping power* [9]. Collisional stopping power results from the energy loss when a charged particle interacts with orbital electrons. Radiative stopping power results from the energy loss through bremsstrahlung radiation as a charged particle interacts with the nucleus of an atom.

Charged particles traveling through an absorber experience Coulomb interactions which can be classified into three groups depending on the classical impact parameter, b, compared to the classical atomic radius, a [9]. The impact parameter is defined as the perpendicular distance between the velocity vector of the particle and the line parallel to that vector which intersects the absorber nucleus. If b is on the order of a, then we will most likely have what is called a hard collision which is a coulomb force interaction between the charged particle and the orbital electrons. When b is larger than a we have a soft collision, where the charged particle is not deflected as much. Finally when b is smaller than a we will have a radiative collision, where the deflection of the charged particle causes a large enough acceleration to release bremsstrahlung radiation [9]. These types of collisions are graphically represented in figure 1–5.

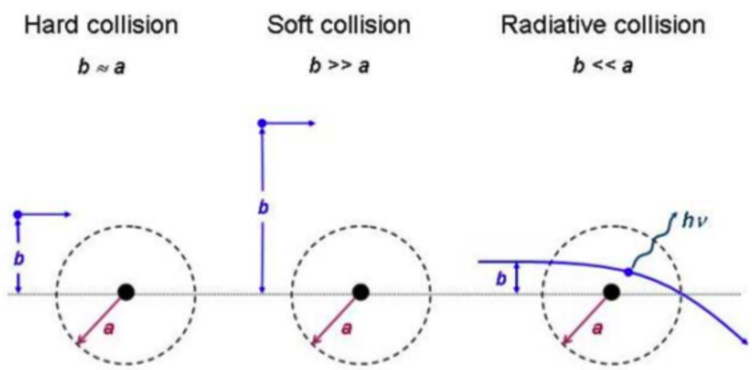

Figure 1–5: Depending on the relative size of the impact parameter, b and atomic radius, a we have different types of collisions that a charged particle can undergo with an atom. A hard collision occurs when $b \approx a$, a soft collision occurs when $b \gg a$ and a radiative collision occurs when $b \ll a$. Reproduced from E.B. Podgorsak, Radiation Physics for Medical Physicists, page 142 [9].

Stopping power can be classified into two subdivisions, collisional (S_{ion}) and radiative (S_{rad}). Stopping power is the energy loss per unit thickness of a medium, $\frac{dE}{dx}$, a more useful quantity is the mass stopping power which is $\frac{1}{\rho}\left(\frac{dE}{dx}\right)$, where ρ is the mass density of the medium. Mass stopping power is usually given in units of MeV/(g/cm^2).

When a charged particle enters a medium, it interacts with the attenuating atoms through ionization and excitation of said atoms. The ionizational mass stopping power equation for electrons can be seen in equation 1.4 and is originally credited to Bethe [4]. The equation takes into consideration both relativistic and quantum mechanical effects.

$$
\begin{aligned}
S_{\text{ion}} &= \frac{1}{\rho}\left(\frac{dE}{dx}\right)_{\text{ion}} &(1.3)\\
&= 2\pi r_0^2 N_{\text{e}} \frac{\mu_0}{\beta^2} &(1.4)\\
&\quad \left[\ln\frac{E^2(E+2\mu_0)}{2\mu_0 I^2} + \frac{E^2/8-(2E+\mu_0)\mu_0\ln 2}{(E+\mu_0)^2} + 1 - \beta^2 - \delta\right]
\end{aligned}
$$

Where r_0 is the classical atomic radius, N_{e} is the electron density, μ_0 is the electron mass expressed as $\mu_0 = m_0c^2$ in (MeV), β is the ratio of the speed of the electron to the speed of light ($\beta = \frac{v}{c}$), I is the mean excitation energy for the absorbing atoms and E is the kinetic energy of the electron. A density correction term, δ is needed to correct for the fact that interactions with distant electrons will be influenced by the electrons in the atoms [4].

Mass collision stopping power is shown for water, aluminum and lead for electrons in the energy range of 10 keV to 100 MeV in figure 1–6.

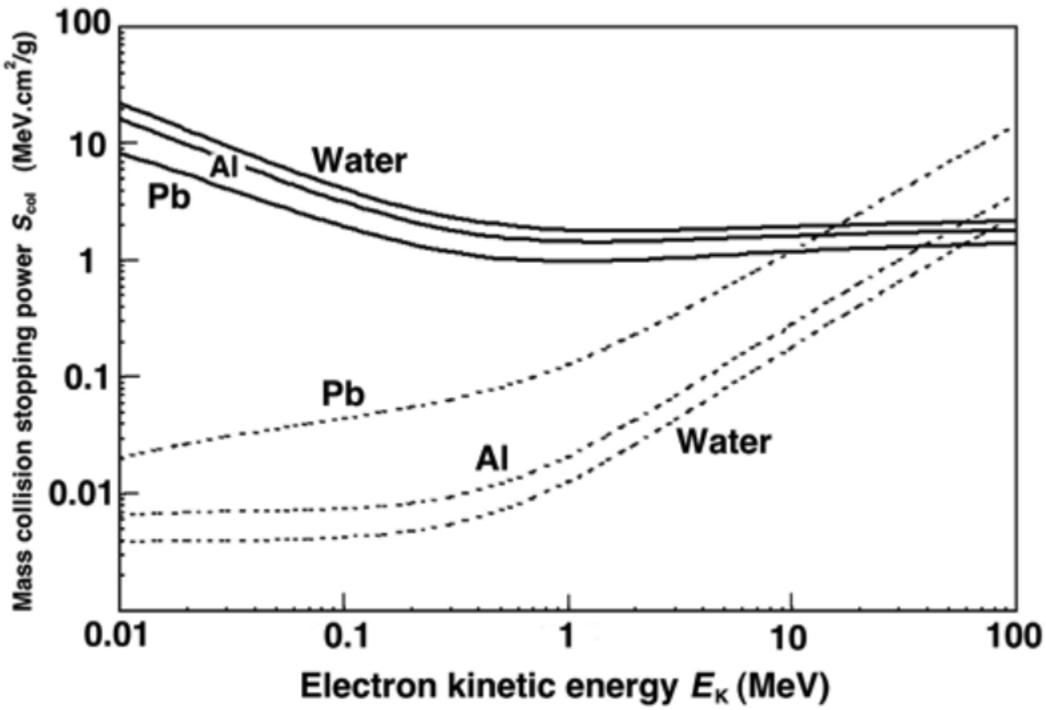

Figure 1–6: Various mass collision stopping power curves for electrons in lead, aluminum and water (solid lines). The dotted lines represent the radiative stopping power for the various materials. Reproduced from E.B. Podgorsak, Radiation Physics for Medical Physicists, page 155 [9].

As previously mentioned, when an electron quickly travels passed an atomic nucleus, it undergoes a coulomb force and will experience an acceleration of roughly $\frac{Ze^2}{4\pi\epsilon_0 r^2 m_e}$. The electron will thus release energy in the form of x-ray radiation called *bremsstrahlung*, german for braking radiation [4]. The equation for radiative stopping power is presented in equation 1.6 [4].

$$S_{rad} = \frac{1}{\rho}\left(\frac{dE}{dx}\right) \tag{1.5}$$

$$S_{rad} = 4r_0^2\frac{N_e ZE}{137}\left[\ln\frac{2(E+\mu_0)}{\mu_0} - \frac{1}{3}\right] \tag{1.6}$$

We also note that the total mass stopping power is the sum of collision and radiative stopping power, $S_{tot} = S_{ion} + S_{rad}$

1.3 Production of Electron Beams

Modern external beam radiotherapy is usually delivered using high energy linear accelerators (linacs). A linac accelerates electrons in a straight line inside of an evacuated structure called a waveguide [8]. High energy radio-frequency fields are used to accelerate the electron inside of the accelerating waveguide (shown in figure 1–7).

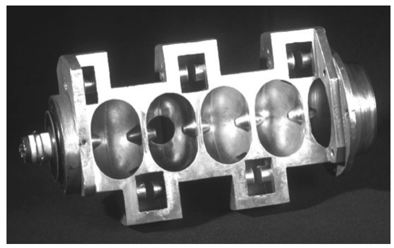

Figure 1–7: Cross section of a 6 MV accelerating waveguide. Reproduced from E.B. Podgorsak, Radiation Oncology Physics: A Handbook for Teachers and Students [8].

RF energy is transferred from the microwave field to the electron in a way such that the area ahead of the electrons appears to have a positive potential, thus continuing to accelerate the electron to higher energies. The frequency of the RF waves is usually 2856 MHz (S band). Linacs typically accerlerate electrons to energies between 4 MeV and 25 MeV [8]. Figure 1–8 shows a diagram of a modern linac.

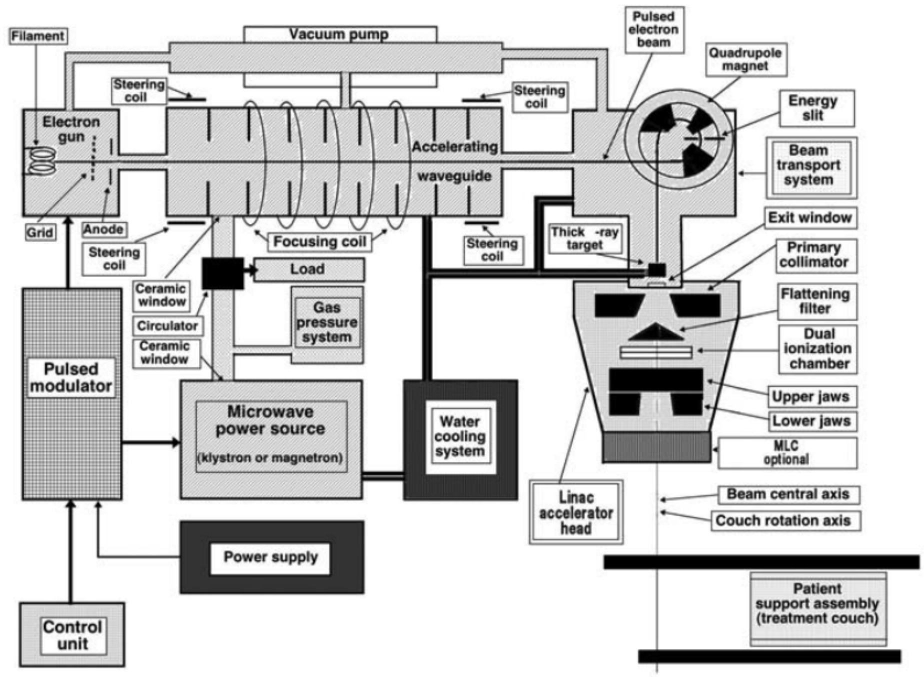

Figure 1–8: Diagram of a modern linac. Reproduced from E.B. Podgorsak, Radiation Oncology Physics: A Handbook for Teachers and Students [8].

When electrons are utilized for radiotherapy, different levels of collimation are required for proper treatment. The primary collimator first collimates the beam to a useful size, then there are movable jaws which further collimate the beam to the field size which is required. After the jaws there are still two levels of collimation which are specific to electron beams. Due to the magnitude of electron scatter in air, it is necessary to keep a relatively flat beam in the centre of the field. This is achieved through the use of an electron applicator (also called cone). The applicator fits in the horseshoe as seen in figure 1–9 and contains scrapers which help block parts of the beam on the edge of the field. The bottom of the applicator has a tray which is used to house the patient specific cutout. The cutout is the final layer of collimation for electron beams and is used to delineate the tumor and to shield the patient's healthy tissue. A typical cutout is shown in figure 1–10

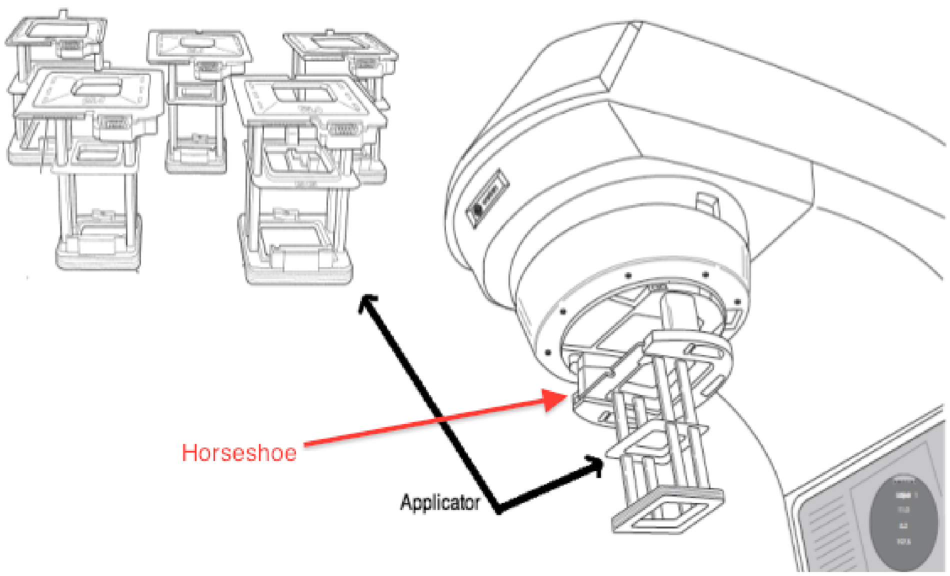

Figure 1–9: Varian CL 21-EX linac with horseshoe and electron applicator mounted. Various applicator sizes are shown in the top left of the figure. Courtesy Varian Medical Systems, Inc. Palo Alto, California.

Figure 1–10: A typical patient-specific cutout insert used to delineate the target and shield the patient.

It is important to note that the presence of a cutout insert will affect the output of the machine. To account for this, an output factor must be measured to ensure the proper treatment of the patient. A typical output factor is measured using a Solid Water® (Gammex RMI, Middleton, WI, USA) phantom with holes drilled at the depths of maximum dose for each electron beam energy and an ionization chamber and electrometer. The output factor is measured as the ratio of accumulated charge in the ionization chamber for the desired cutout at desired SSD to the charge for a reference cutout at 100 cm SSD. In each case the chamber is placed at z_{max} for the energy being used. The following equation summarizes the definition of the output factor:

$$\mathrm{OF} = \frac{D_i(z_{\mathrm{max}}, A, f, E)}{D_{\mathrm{ref}}(z_{\mathrm{max}}, 10 \times 10\ \mathrm{cm}^2, 100\ \mathrm{cm}, E)} \times 100 \tag{1.7}$$

Where D_i is the dose at z_{max} for the desired cutout field using the chosen energy and SSD, D_{ref} is the dose at z_{max} for the reference field which is a square cutout with dimensions of 10×10 cm^2 (figure 1–11), f is the SSD for the treatment and E is the treatment energy.

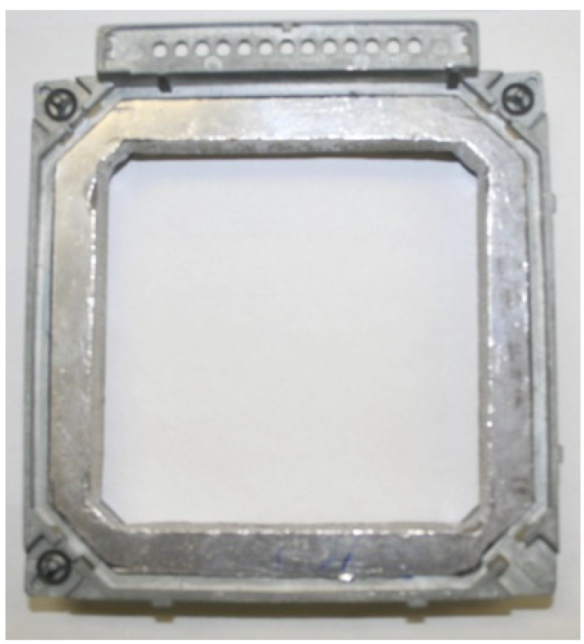

Figure 1–11: 10×10 cm^2 reference cutout used for clinical output factor measurements.

The linacs used in this study are the Varian Clinac 21-EX and Clinac iX (Varian Medical Systems, Palo Alto, CA), they each come with a set of applicators with sizes of 6×6 cm^2, 10×10 cm^2, 15×15 cm^2, 20×20 cm^2 and 25×25 cm^2. Each applicator size and energy pair require a different set of jaw settings. These settings are listed by the manufacturer and are to ensure that the electron beam is flat in the centre of the beam once it gets collimated down to the correct size. The settings are listed in table 1–1.

Applicator	6, 9 MeV	12 MeV	16 MeV	20 MeV
6×6 cm^2	20×20 cm^2	11×11 cm^2	11×11 cm^2	11×11 cm^2
10×10 cm^2	20×20 cm^2	14×14 cm^2	14×14 cm^2	14×14 cm^2
15×15 cm^2	20×20 cm^2	17×17 cm^2	17×17 cm^2	17×17 cm^2
20×20 cm^2	25×25 cm^2	25×25 cm^2	23×23 cm^2	22×22 cm^2
25×25 cm^2	30×30 cm^2	30×30 cm^2	28×28 cm^2	27×27 cm^2

Table 1–1: Linac jaw settings for a given applicator and energy combination for Varian Cinac 21-EX and Clinac iX machines.

1.4 Electron Beam Treatment Planning

The most commonly used dose distribution for electron beam treatment planning (TP) is the central axis dose distribution as described in figure 1–2 in section 1.1. This is the most straightforward method and is used since usually single fields are used [7]. This poses a problem however when patient geometry and tissue inhomogeneities are taken into consideration. Electron PDDs are measured in water or water like material at normal incidence, obliquity will cause the PDD to change significantly, as seen in figure 1–4. Heterogeneities within the patient will also cause the dose distribution to differ from that of a water phantom.

The most useful dosimetric quantities used in electron beam TP are [7]:

- Skin dose
- Initial build up of dose with depth
- The depth of maximum dose ($d_{\max}$)

- The uniformity of dose across the beam
- Central plane isodose distributions

These quantities are typically used for electron beam TP, for example the energy might be selected, such that the tumor is covered by the 90% isodose line, thus R_{80} would be used to determine what energy to use for the plan.

The most commonly used beam specifier for electrons is the incident surface energy, E_0. E_0 is very often determined using the empirical relationship with the practical range, R_p as described by the Markus equation [6].

$$R_\mathrm{p} = 0.521 \left[\frac{\mathrm{cm}}{\mathrm{MeV}}\right] E_0 - 0.376\,[\mathrm{cm}] \tag{1.8}$$

The Markus equation is valid to within 2% for electron energies from 5 to 40 MeV [7].

Electron beams have little to no skin sparing properties since the skin dose for a typical beam is in the range of 85-95%. Low energy, scattered electrons are introduced due to the presence of scattering foils and collimation systems, this has the effect of increasing the surface dose of a beam and shifting the depth of maximum dose towards the surface [10]. Bremsstrahlung photons are also generated through the collimation system and the magnitude of photon contamination depends on the thickness and material of the scattering foil being used [7]. The locations of the depths of dose maximum for the machines used in this study are listed in table 1–2 for each energy and applicator size. Although the location of z_max may fluctuate between 2-3 cm for 12, 16 and 20 MeV, for practicality the majority of output factor measurements are performed at 3.0 cm within a Solid Water® phantom for those energies.

The effect of inhomogeneities on electron dose distributions can be appreciable and several attempts have been made to account for this. Absorption of electrons

Applicator Size	6 MeV	9 MeV	12 MeV	16 MeV	20 MeV
6×6 cm^2	1.3 cm	2.0 cm	3.0 cm	2.5 cm	2.0 cm
10×10 cm^2	1.3 cm	2.0 cm	3.0 cm	3.0 cm	2.0 cm
15×15 cm^2	1.3 cm	2.0 cm	3.0 cm	3.5 cm	2.0 cm
20×20 cm^2	1.3 cm	2.0 cm	3.0 cm	3.0 cm	2.0 cm
25×25 cm^2	1.3 cm	2.0 cm	3.0 cm	3.0 cm	2.0 cm

Table 1–2: Depth of maximum dose for each energy and applicator size on the Jewish General Hospital's Varian CL21-EX linear accelerator used in this study. The data was acquired during commissioning of the machine by physicists at the JGH.

is determined primarily by the electron density of the medium, however electron scatter depends strongly upon atomic number [1]. The dose distribution also depends on the range of the electrons, which is inversely proportional to the density of the irradiated material [1]. Several clinical situations will arise where the dose is needed and it is required to account for inhomogeneities, for example when one requires the dose in soft tissue beyond a heterogeneity or within the heterogeneity itself [7]. In the early years of electron treatment planning, several attempts had been made to correct for inhomogeneities [7]; namely, the absorption equivalent thickness (AET) method of Laughlin [5], the electron absorption coefficient of Dahler et al. [3], the coefficient of equivalent thickness (CET) of Almond et al. [1] and the modified absorption coefficient of Bagne [2]. It is clear that when using solely 1D dose data for treatment planning as is typically the case, no inhomogeneity correction is applied and this could lead to inaccurate patient dose.

1.5 Proposed Work

This research project was developed to gauge the efficacy of using a Monte Carlo (MC) system for electron cutout output factor calculations and electron treatment planning. To do so, a series of cutout output factor measurements and calculations for different energies and applicator sizes will provide a measure of error between measurements and calculations. Profile measurements in a Solid

Water® phantom are compared to MC calculated profiles. Film measurements in two heterogenous phantoms are performed for 2D analysis of the MC calculation's heterogenous performance.

1.6 Scope and Structure of Thesis

Chapter 2 provides an overview of the Monte Carlo method and describes the Monte Carlo codes pertinent to this work: BEAMnrc, DOSXYZnrc and CUTOUT. Descriptions of the McGill Monte Carlo Treatment Planning (MMCTP) system which is used for MC patient treatment planning and the Cutout Manager graphical user interface (GUI) which is used for output factor calculation job submission and database manager are also provided. **Chapter 3** describes the dosimetric devices used in this study. Of the many dosimetric devices available for clinical medical physics use, those that are dealt with in this study include Solid Water®, ionization chambers, the IBA Blue phantom and Gafchromic film. In **Chapter 4**, a comparison of measured and MC calculated electron cutout output factors is presented for various energies and applicator sizes. **Chapter 5** discusses the profile comparisons for two custom designed cutouts for electron beams in a Solid Water® phantom. The profiles were obtained at two different depths (d_{max} and R_{50}) for 6, 9, 12, 16 and 20 MeV electron beams. **Chapter 6** deals with the two heterogeneous phantoms and the film analysis and comparison for the different electron beam energies. Finally, **Chapter 7** provides some final remarks and future considerations for this work.

References

[1] P.R. Almond, A.E. Wright, and M.L.M Boone. High energy electron dose perturbations in regions of tissue heterogeneity. *Radiol.*, 1967.

[2] F. Bagne. Electron beam treatment-planning system. *Med. Phys.*, 1976.

[3] A. Dahler, A.S. Baker, and J.S. Laughlin. Comprehensive electron bea treatment planning. *Ann. N.Y. Acad. Sci*, 1969.

[4] H.E. Johns and J.R. Cunningham. *The Physics of Radiology*. Thomas, fourth edition, 1983.

[5] J.S. Laughlin. High energy electron treatment planning for inhomogeneities. *British Journal of Radiology*, 38(143), 1965.

[6] B. Markus. Energiebestimmung schneller elektronen aus tiefendosiskurben. *Strahlentherapie*, 1961.

[7] C.G. Orton and F. Bagne, editors. *Practical Aspects of Electron Beam Treatment Planning*. American Association of Physicists in Medicine, American Institute of Physics, 1978.

[8] E. B. Podgorsak, editor. *Radiation Oncology Physics: A Handbook for Teachers and Students*. International Atomic Energy Agency, Vienna, 2005.

[9] E. B. Podgorsak. *Radiation Physics for Medical Physicists*. Springer, first edition, 2006.

[10] H. Svensson and G. Hettinger. The influence of the collimating system on the dose distribution from 10 to 35 mev electron radiation. *Acta Radiologica*, 1967.

CHAPTER 2
The Monte Carlo Method

Contents

2.1 Introduction

Over the past fifty years, Monte Carlo (MC) techniques have become prevalent within the medical physics community. In his review of Monte Carlo in medical physics [7], Rogers indicates that there has been a doubling of papers including the term 'Monte Carlo' in the title or abstract in either *Physics in Medicine and Biology* or *Medical Physics* every five years between 1967-2000. This exponential increase in use is due to the increase in computing power to cost ratio that we have experienced as well as the availability of powerful MC programs [7]. Although there are different variations of the MC method, generally MC uses random variables created by a random number generator (RNG) to sample probability density functions (PDF) to predict particular outcomes of a given system. For applications in the medical physics field, MC uses interaction cross section data to formulate the PDFs to be sampled and uses random variables to determine what interaction type is undergone at each step of the simulation.

2.2 Radiation Transport

In simulating photon transport through a medium, MC programs randomly determine the step length, s a photon will travel before undergoing an interaction as determined in equation 2.1 [2]. Once the step length has been determined, the type of interaction is determined by sampling a probability density function (PDF) using another random variable.

$$s = -\lambda \ln (1 - \xi) \tag{2.1}$$

Where s is the path length, λ is the mean free path and ξ is a random number in the range $0 \leq \xi < 1$. The mean free path is the average distance a photon travels in an absorber before undergoing an interaction. We note that the mean free path is defined as:

$$\lambda = \frac{A}{N_{\mathrm{a}} \rho_{\mathrm{a}} \sigma_{\mathrm{t}}} \tag{2.2}$$

Where A is the atomic mass of the absorber atoms, N_{a} is Avogadro's number, ρ is the mass density of the absorber and ${}_{\mathrm{a}}\sigma_{\mathrm{t}}$ is the total atomic cross section of all the interactions for photons, namely

$${}_{\mathrm{a}}\sigma_{\mathrm{t}} = {}_{\mathrm{a}}\tau + {}_{\mathrm{a}}\sigma_{\mathrm{c}} + {}_{\mathrm{a}}\kappa + {}_{\mathrm{a}}\sigma_{\mathrm{R}} \tag{2.3}$$

where

${}_{\mathrm{a}}\tau$ is the total cross section for the photoelectric effect.

${}_{\mathrm{a}}\sigma_{\mathrm{c}}$ is the total cross section for Compton scattering.

${}_{\mathrm{a}}\kappa$ is the total cross section for pair production.

${}_{\mathrm{a}}\sigma_{\mathrm{R}}$ is the total cross section for Rayleigh scattering.

Once the step size is found, the type of interaction is determined by sampling from the appropriate relative probability of interactions, p_i [2]. p_i is the ratio of an interaction's single cross section to the total cross section for the absorber atom:

$$p_i = \frac{1}{{}_{\mathrm{a}}\sigma_{\mathrm{t}}} \sum_{j=1}^{i} {}_{\mathrm{a}}\sigma_j \tag{2.4}$$

The interaction cross section is energy and atomic number dependent, we thus describe three regions of interaction predominance in the medical physics field. Figure 2–1 displays the regions of predominance of photoelectric effect, Compton effect and pair production effect as a function of photon energy, $h\nu$ and atomic number, Z. The region to the left of the ${}_{\mathrm{a}}\tau = {}_{\mathrm{a}}\sigma_{\mathrm{c}}$ line is photoelectric effect predominated, between the ${}_{\mathrm{a}}\tau = {}_{\mathrm{a}}\sigma_{\mathrm{c}}$ and ${}_{\mathrm{a}}\sigma_{\mathrm{c}} = {}_{\mathrm{a}}\kappa$ lines is Compton effect predominated and to the right of the ${}_{\mathrm{a}}\sigma_{\mathrm{c}} = {}_{\mathrm{a}}\kappa$ line is the region of pair production predominance. Due to the low effective atomic number of tissue and the relatively high photon energies used in radiotherapy, the main photon interactions occurring during a megavoltage (MV) beam treatment are the Compton effect and pair production.

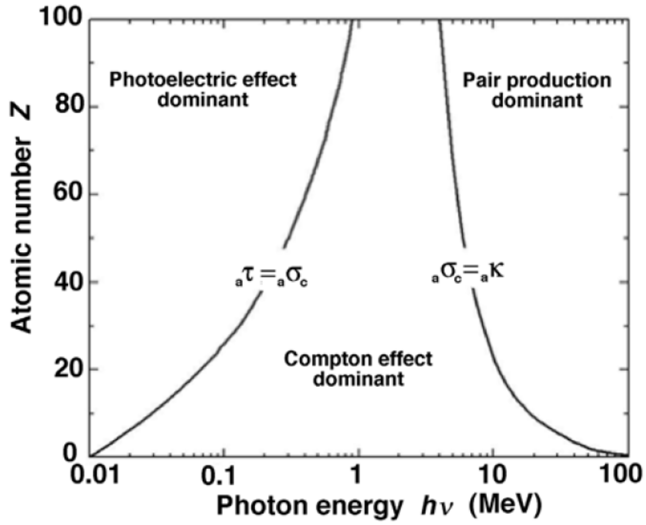

Figure 2–1: Regions of photon interaction type predominance as a function of both atomic number and photon energy. Reproduced from E.B. Podgorsak, Radiation Physics for Medical Physicists, page 246 [6].

Another random number ξ selects the interaction type, $i(\xi)$ such that

$$\sum_{i=1}^{j-1} p_i = P_{j-1} \leq \xi < \sum_{i=1}^{j} p_i = P_j \tag{2.5}$$

where $i(\xi)$ is the Rayleigh, photoelectric, Compton or pair production effect at the corresponding photon energy [2]. This process is continued until the photon loses all of its energy or leaves the geometry in question.

Electrons undergo thousands of elastic interactions as they penetrate a medium [4]. The electrons lose their energy via two main processes, inelastic collisions with the absorber's atoms or molecules and radiative interactions. The inelastic collisions result in excitations and ionizations of the absorber atoms. Ionizations can lead to secondary electrons being set in motion, which are referred to as δ particles [4]. An electron can also lose energy in the form of radiation via bremsstrahlung or positron annihilation. Keeping track of every interaction that occurs for electron transport would take a very long time and very powerful processors. To speed up the calculation while retaining good accuracy, the condensed history (CH) technique is employed. The CH technique was first developed by Berger in 1962 [3], where many interactions get condensed into groups to form short steps. Since so little energy gets released for a given interaction, this method is a good approximation and greatly increases the speed of the calculation.

2.3 MC codes

2.3.1 Linear Accelerator Simulations using BEAMnrc

In 1995 D.W.O Rogers et al. of National Research Council Canada (NRC) published a paper titled *BEAM: A Monte Carlo code to simulate radiotherapy treatment units* [8]. This paper describes the NRC's solution to simulating radiation beams from radiotherapy treatment units such as a linear accelerator. BEAM was a MC user code that ran on top of the EGS4 code system. The current version of BEAM is BEAMnrc and it runs on the EGSnrc system [5].

For linacs, BEAMnrc uses virtual component modules (CM) to model each of the element in the linac head. The following is a list of the main CMs used in linac modeling.

SLABS

Models parallel slabs in the x-y planes with arbitrary thickness and material.

CONS3R

Models a stack of truncated cones. Useful for modeling flattening filters where the inner region is a heavy material and the outer region is air.

FLATFILT

Models the beam flattening filters used in photon beam simulations.

CHAMBER

Models a parallel plate ionization chamber with top and bottom plates with user defined thickness and material.

JAWS

Models sets of paired jaws for collimation. The angle is also user definable.

APPLICAT

Models a set of rectangular scrapers used in electron beam applicators.

DYNVMLC

Models a Varian Millennium MLC.

MIRROR

Used to simulate mirrors in the accelerator head. The mirror consists of one or more flat layers of different materials.

In using BEAMnrc, the user creates a virtual linac by compiling a file which contains the CMs needed for the particular machine in the order that they are required in. The user then generates a preference file which contains the necessary parameters for the specific machine. These parameters include information on the geometries of all the CMs within the linac, the energy spectrum used, number of histories required and any special options that the user might desire. To create a custom machine the user may begin with a template, compare the results with measurements and iteratively adjust certain parameters until the beam model satisfies the measurements. The work presented in this thesis uses an electron beam model of a Varian (Varian Medical Systems, Palo Alto, CA) Clinac 21EX linear accelerator created and commissioned by Jonathan Thébaut through his Master's thesis work at McGill University [10]. Figure 2–2 is a graphical representation of the BEAMnrc model for electron therapy used in this work.

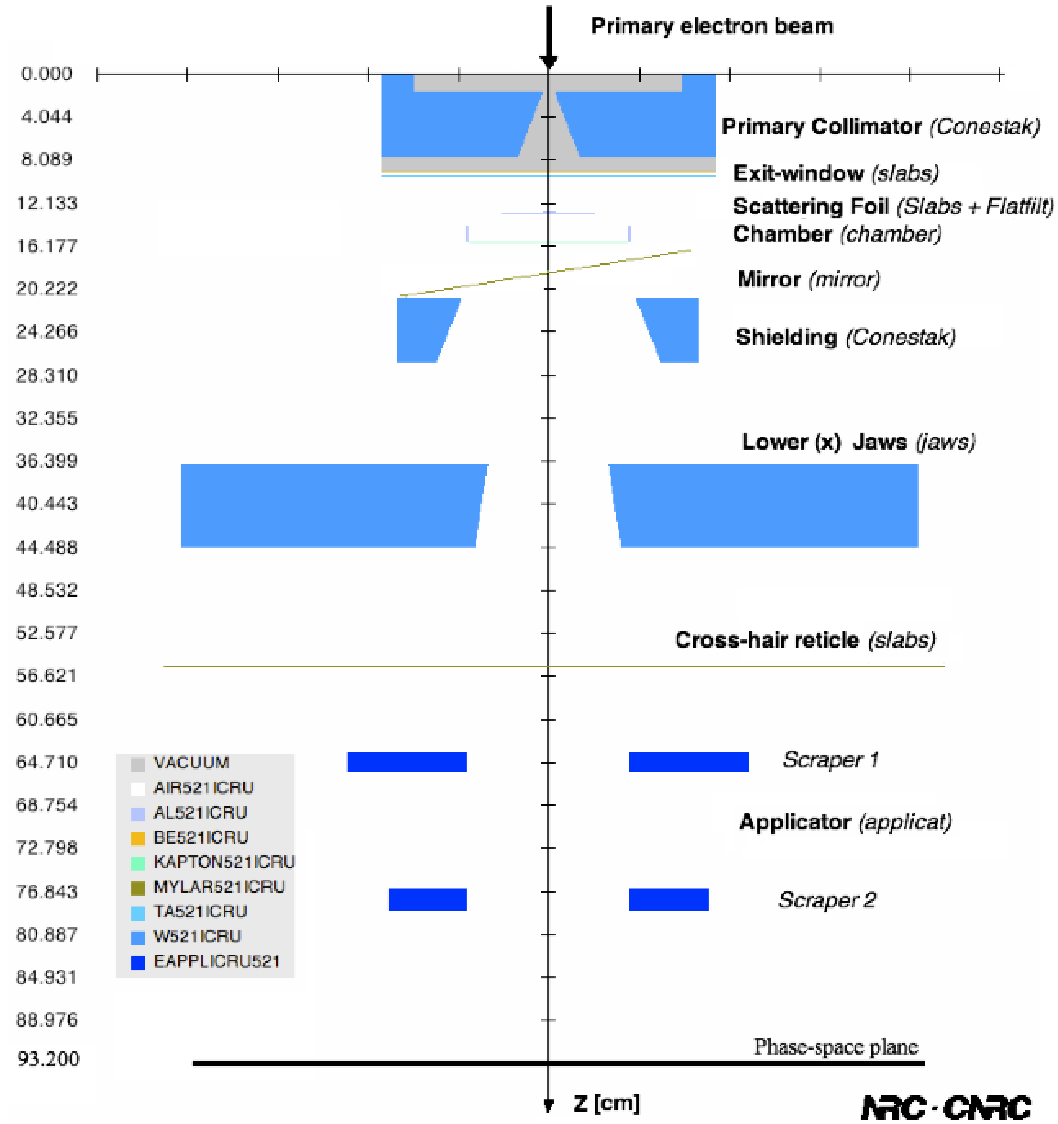

Figure 2–2: Schematic representation of the Varian CL21EX linac modeled using BEAMnrc. Each CM is labeled with a name and the type of CM it is in parentheses. The Z axis is shown for scale and is in units of cm. The patient specific cutout would be inserted at the bottom of the treatment head, with the cutout located between 93.2 and 95 cm. Courtesy of Jonathan Thébaut via the BEAMnrc GUI.

BEAMnrc jobs are submitted by specifying the input file (`.egsinp`), a PEGS4 data file and a location for the phase-space file (PSF). The PEGS4 file contains densities and cross section data for all the materials within the CMs for many different energies. The PSF contains data relating to particle position, direction, momentum, charge, etc. for each particle crossing a scoring plane [9]. A PSF can be requested at any scoring plane the user desires and more than one can be generated as well, each at a different scoring plane. Provided the linac treatment head does not change for a given beam, once a PSF has been generated, it need not be generated again. The PSF can be reused for whatever need the user may have of it. For example, for a given energy and applicator size, only one PSF needs to be generated and this PSF can be reused in determining the beam that would occur if it were to pass through a patient specific cutout (see section 2.3.3). The PSF from BEAMnrc can also be used to determine dose within a CT phantom through DOSXYZnrc.

2.3.2 Patient Dosimetry Calculations using DOSXYZnrc

DOSXYZnrc is a MC EGSnrc user-code used for 3-dimensional absorbed dose calculations within a rectilinear volume element (voxel) phantom [11]. The voxel dimensions are user definable in either direction (x,y,z) and can have different materials. To convert patient CT data to a virtual phantom compatible with DOSXYZnrc, a program called `ctcreate` is used.

There are different ways that the geometries can be setup in DOSZYZnrc, in this work we use a polar coordinate system at the isocenter using the origin, xiso, yiso, ziso (`ISOURCE=2`). The position of the origin in the phase-space plane is then defined by the angles theta and phi [11]. Figure 2–3 depicts this geometry of the phase-space plane relative to the clinical coordinate system.

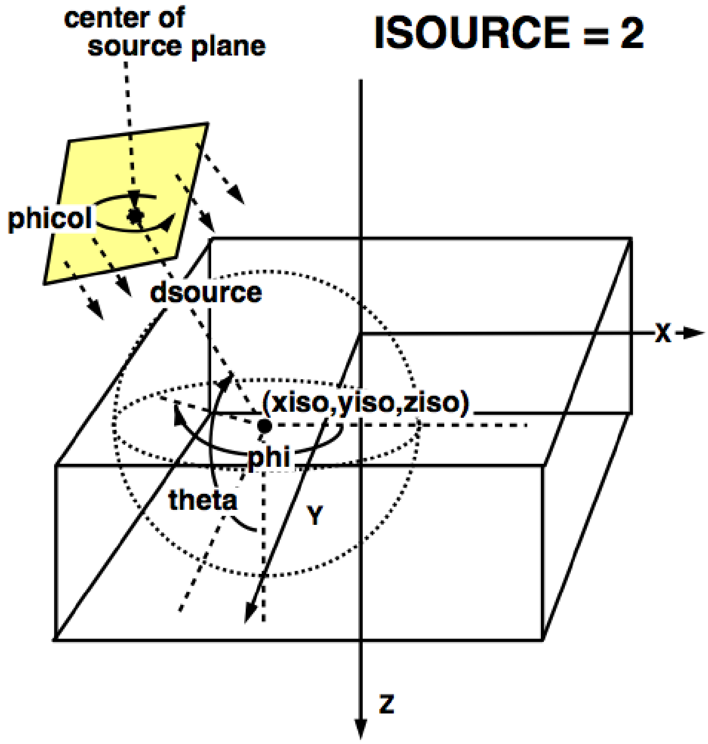

Figure 2–3: In ISOURCE=2 calculations, the phase-space plane is arbitrarily positioned in space. A polar coordinate system is set up with the origin at the isocenter. The origin of the phase-space plane is then defined by the angles theta and phi and the distance from the isocenter, dsource.

2.3.3 Cutout Insert Simulation in CUTOUT

The CUTOUT code is an EGSnrc based user code written in mortran which is designed to transport phase-space particles through a layer of arbitrarily shaped electron cutout material. The input of the code is an electron beam PSF with the scoring plane above the top cutout plate. The user can define the material and thickness of the given cutout for each of the calculations. To use the system, reference fields must first be simulated in BEAMnrc and run through CUTOUT. The reference fields consist of the standard 10×10 cm^2 cutout insert along with the correct jaw and applicator geometries. Once the reference fields have been simulated through CUTOUT, the maximum dose batch data is obtained and placed in a preference file for each given energy and linear accelerator. This is necessary so that when an output factor is desired, the system will use these reference doses for the normalization. If other linacs are to be used, the process of gathering reference field data must be repeated for each machine.

A graphical user interface (GUI), called Cutout Manager was created to simplify the submission of CUTOUT jobs and help manage the ensuing data. The user creates each individual CUTOUT job by defining the necessary parameters (energy, applicator size, SSD, patient name, etc.) and digitizing the cutout. The main Cutout Manager window is shown in figure 2–6, in this window, the user can see each of the cutout entries that were created as well as the output factor calculation results.

The process of digitizing the cutout consists of tracing the outline of the cutout opening on a piece of paper (1:1 scale), the sheet is placed on the monitor with the digitization window open and the user defines a polygon by clicking on the edge of the cutout outline. The more points used in the digitization, the more accurately the polygon will model the cutout. The Cutout Manager digitization window is shown in figure 2–4. It is also possible to select the origin in the digitization window in the cases where the centre of the cutout tray is not where the output factor is to be determined.

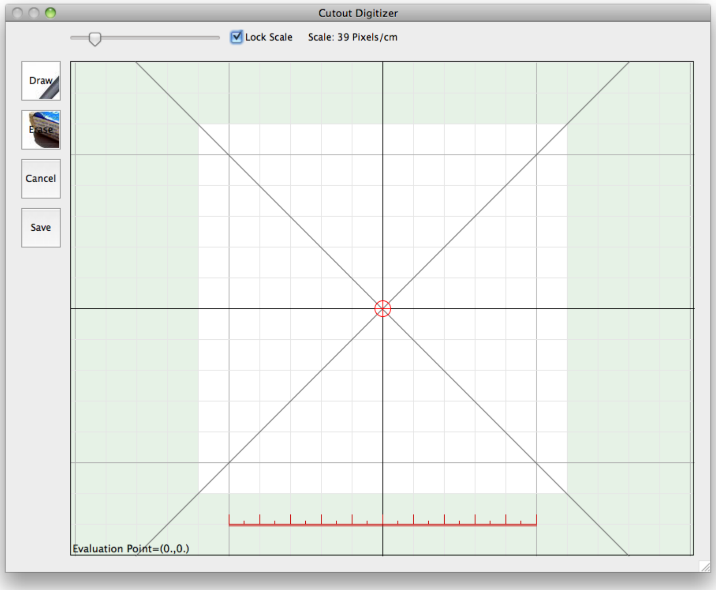

Figure 2–4: The cutout digitizer window is where the user digitizes the physical cutout. The cutout is traced onto a piece of paper and then held up to this window where the user defines points on the periphery of the traced cutout. For this system to be accurate, the window must be calibrated for the specific monitor used. This is accomplished by placing a ruler beneath the red ruler markings at the bottom of the window and adjusting the scale slider above until it measures 10 cm. The red crosshairs in the centre of the grid can be moved by the user, this defines a new origin of the system.

Once the cutout is digitized, the user then has the choice between obtaining an output factor or a PSF at the end of the cutout insert (or obtaining both). To submit a job, the user simply creates the case in the Cutout Manager workbench (figure 2–5) and executes the submission through the Cutout Manager main window (figure 2–6).

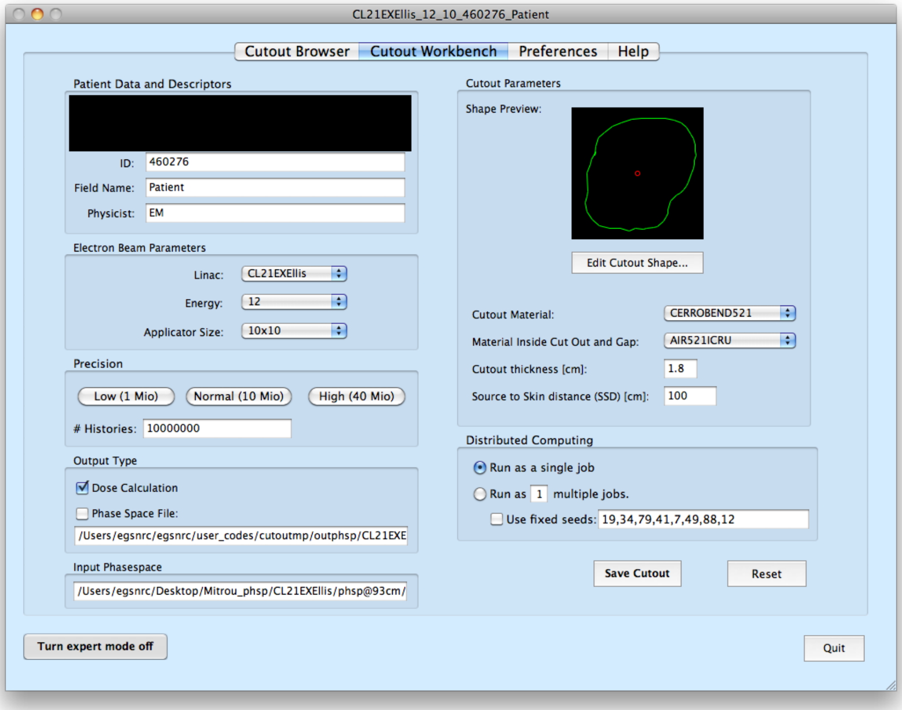

Figure 2–5: The Cutout Manager Workbench is where the user inputs all the necessary parameters for a new cutout output factor job submission. It is here where beam energy, applicator size, linac, etc. are selected.

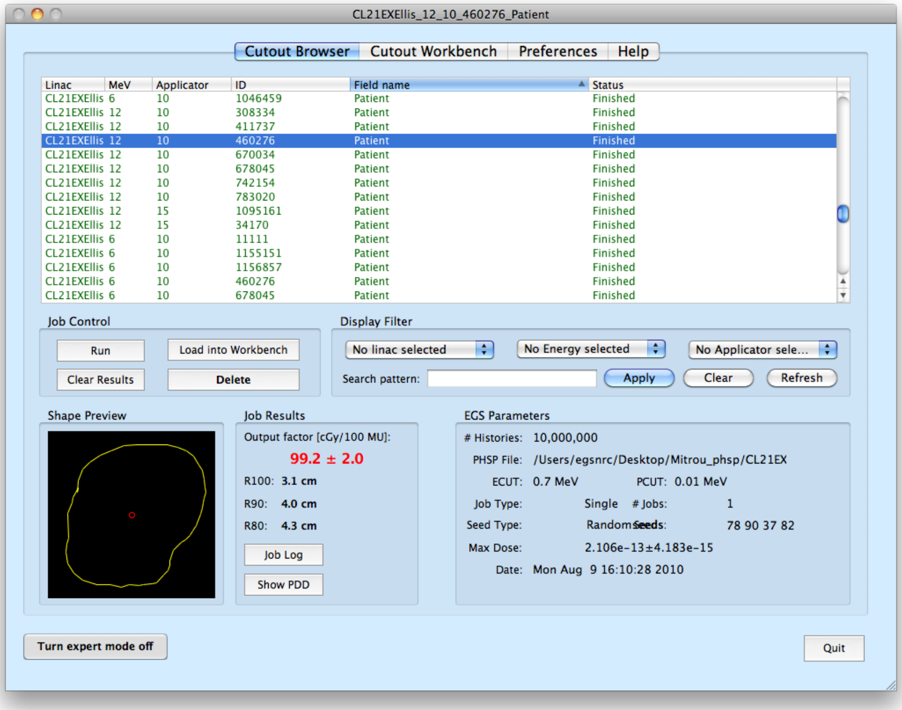

Figure 2–6: The main Cutout Manager window allows the user to view the catalogue of previously calculated cutout output factors, submit new jobs and monitor current calculations.

The GUI then creates a .egsinp file and submits all the required bash commands and constantly updates the results until completion. For an output factor, once the job is done, the maximum dose in a cylindrical phantom with specified SSD is determined along the beam's central axis, or another user defined axis. This dose is normalized to the reference field; the result defines the cutout output factor. For phase-space output, the phase-space file is placed in the cutout folder and can be used as desired.

To simplify the use of CUTOUT, the linac treatment head PSFs for each energy and applicator size combination were obtained before-hand using BEAMnrc. This was done for electron beam energies of 6, 9, 12, 16 and 20 MeV and for applicator sizes of 6×6, 10×10, 15×15 and 20×20 cm^2. The jaw dimensions used for each of these cases are tabulated in table 1–1 on page 13.

2.3.4 Streamlining the Process through MMCTP

The McGill Monte Carlo Treatment Planning (MMCTP) environment was developed at McGill University by Alexander et al. [1] to serve as a full-featured MC treatment planning system, a screenshot of the MMCTP environment is shown in figure 2–7.

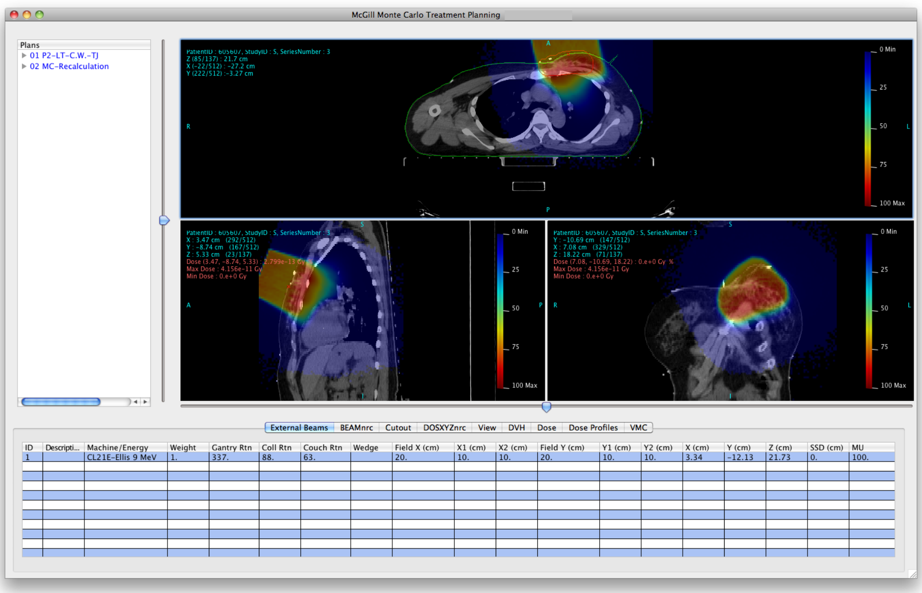

Figure 2–7: Main treatment planning window in MMCTP. In this pane, the user can add treatment machines and define certain beam geometries such as field size and SSD. The plans are listed in the top left portion of the window, and any dose distribution that has been imported or calculated can be selected there. In the centre of the window is the CT and dose distribution viewer. A recalculated breast cancer case is shown with the GTV outlined in red.

MMCTP runs on the EGSnrc system and drastically simplifies the lives of those brave enough to venture into the world of MC based medical physics calculations. MMCTP submits jobs to networked workstations via standard secure-shell (SSH) protocol to run the calculations [1]. MMCTP interfaces with BEAMnrc, DOSXYZnrc and CUTOUT on the workstation in question as long as the workstation is properly configured. For example, if the user wishes to submit a BEAMnrc job to a computer somewhere on the clinic's network or through the world wide web, the accelerator executable must be made on that computer and the credentials for the user account must be specified in the MMCTP preferences. The fact that the user codes with which the user wants to use need not be on the computer running MMCTP is a powerful feature of MMCTP. This allows a clinic or research institution to have a devoted cluster of computers which several users can submit to simultaneously. In this study MMCTP ran on an 8 CPU core Mac Pro with 2×2.8 GHz Quad core Intel Xenon Processor and 10 GB RAM (Apple Inc., Cupertino, California) and submitted jobs to itself as well as to two other dual CPU core iMacs within the department. Figure 2–8 depicts the diagram of the server setup which was used in this study.

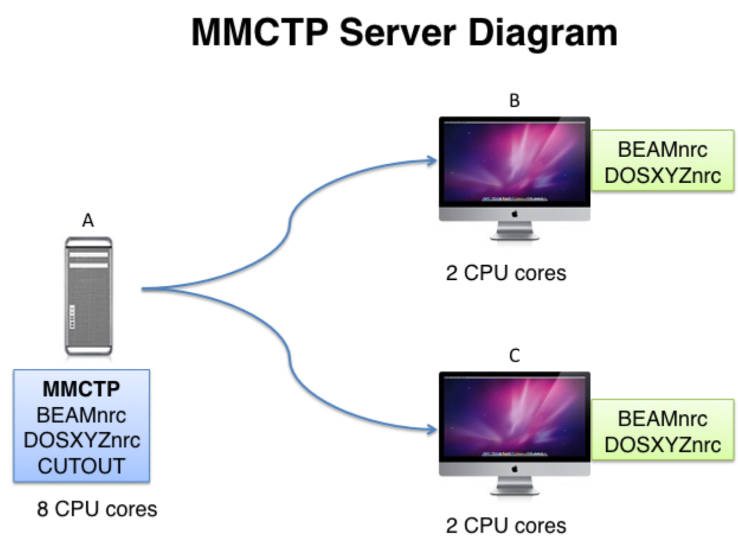

Figure 2–8: Diagram of the MMCTP server which was used in this study. The controller computer was an 8 Core Apple Mac Pro and this communicated with two dual core iMacs which had BEAMnrc and DOSXYZnrc installed. MMCTP was configured on the Mac Pro which was able to submit jobs to itself as well. The Mac Pro was the sole to have CUTOUT installed for cutout output factor or PSF calculations.

References

[1] A. Alexander, F. DeBlois, G. Stroian, K. Al-Yahya, E. Heath, and J. Seuntjens. Mmctp: a radiotherapy research environment for monte carlo and patient-specific treatment planning. *Physics in Medicine and Biology*, 2007.

[2] P. Andreo. Monte carlo techniques in medical radiation physics. *Phys. Med. Biol.*, 36(7):861–920, 1991.

[3] J. Berger. Monte carclo calculation of the penetration and diffusion of fast charged particles. *Methods in Computational Physics*, 1963.

[4] I. J. Chetty et al. Report of the aapm task group no. 105: Issure associated with clinical implementation of monte carlo-based poton and electron external beam treatment planning. Technical report, AAPM, 2007.

[5] I. Kawrakow and D. W. O. Rogers. The egsnrc code system: Monte carlo simulation of electron and photon transport. Technical report, National Research Council of Canada, 2006.

[6] E. B. Podgorsak. *Radiation Physics for Medical Physicists*. Springer, first edition, 2006.

[7] D. W. O. Rogers. Fifty years of monte carlo simulations for medical physics. *Phys. Med. Biol.*, 51:287–301, 2006.

[8] D. W. O. Rogers, B. A. Faddegon, G. X. Ding, C.-M Ma, and J. We. Beam: A monte carlo code to simulate radiotherapy treatment units. *Med. Phys.*, 22(5):504–523, May 1995.

[9] D. W. O. Rogers, B. Walters, and I. Kawrakow. *BEAMnrc User's Manual*. NRC, 2009.

[10] J. Thébaut. Measurement driven, electron beam modeling and commissioning for a monte carlo treatment planning system with improved accuracy. Master's thesis, McGill University, 2009.

[11] B. Walters. *DOSXYZnrc Users Manual*. NRC, 2009.

CHAPTER 3
Dosimetric Devices

Contents

3.1 Introduction

A radiation dosimeter is a device which measures, either directly or indirectly, certain quantities such as exposure, kerma, absorbed dose or a related characteristic of ionizing radiation [4]. Certain physical aspects of the dosimeter must be a function of the desired quantity to be measured and once calibrated can be used to measure it. A good dosimeter has good precision and accuracy, demonstrates linearity and is both energy and dose rate independent. Due to real world constraints, it is very difficult to have a dosimetric system with all the aforementioned qualities, so certain compromises are made. For example, due to its high spatial resolution and 2D nature, film dosimetry is ideal for the measurement of 2D dose distributions, its lower accuracy relative to ionization chambers however make film less suitable for beam calibration. The dosimetric devices used in this study include ionization chambers, film dosimeters, Solid Water® phantoms and 3D water phantoms.

3.2 Solid Water®

Water is the standard reference material for dosimetry, it is a good approximation to human tissue since tissue is mostly water to begin with. Using water in a clinical setting, however, is cumbersome and requires waterproof dosimeters. For these reasons, a material known as Solid Water® (Gammex RMI, Middleton, WI, USA) was developed by Constantinou [2] to mimic the abosorption characteristics of water over a wide range of energy [1]. Today, Solid Water® is manufactured by Gammex and is claimed to permit achieving calibrations within 1% of the true water dose.

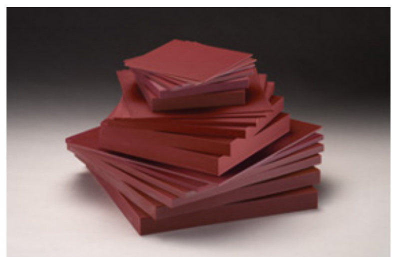

Figure 3–1: Solid Water® slabs of various sizes. Manufactured by Gammex, Inc., Middleton, WI. Reproduced from reference [1]

In this study, Solid Water® is used to perform output factor calculations. The Solid Water® has holes drilled in for the insertion of an ionization chamber at the nominal depths of dose maximum for each electron energy. Solid Water® is also found in two heterogeneous phantoms to simulate soft tissue.

3.3 Ionization Chambers

A Farmer type ionization chamber consists of a gas filled cavity surrounded by a conductive outer wall with a central collecting electrode [4]. When in operation, the central electrode of an ion chamber is kept at a high voltage (±300 V) and the outer electrode is kept at 0 V. When a high energy particle ionizes the gas within the chamber, the ions get attracted to the electrodes, where they either deposit (in the case of a negative ion) or receive (in the case of a positive ion) an electron from the electrode. This neutralizes the ion but creates a detectible current which is measured by an electrometer. A PTW TN30011 Farmer type ionization chamber (PTW, Freiburg, Germany) was used for the output factor measurements in this work. The collecting volume of this chamber is 0.6 cm^3. The chamber is coupled to a Fluke electrometer (Fluke Biomedical, Everett, WA).

3.4 IBA Blue Phantom

To acquire electron beam profile data, an IBA Blue phantom (IBA, Louvain-la-Neuve, Belgium) was used. The Blue phantom uses DC motors to move the detector through the tank. The setup of the chamber is performed using a hand pendant device connected to the phantom. Once the chamber is put in place, it is zeroed to create an origin of reference. The technical specifications of the phantom are found in table 3–1.

Scanning Volume (LxWxH)	480 mm x 645 mm x 560 mm (≈ 200 L)
Position resolution	0.1 mm
Max. scanning speed	50 mm/s
Mass	45 kg
Wall thickness and material	15 mm / acrylic

Table 3–1: Technical specifications of the IBA Blue phantom as described by the manufacturer in the phantom brochure.

3.5 GAFCHROMIC® EBT2 Film

GAFCHROMIC® EBT2 Film (ISP, Wayne, NJ, USA) was used for 2D electron dosimetry in the heterogeneous phantoms (see **chapter 6**). The film was calibrated by irradiating small pieces of film with a 6 MV photon beam for doses ranging from 0 to 500 cGy. The films were scanned using an Epson Expression 10000XL document scanner (Epson, Tokyo, Japan) following the protocol described in Devic et al. (2005) [3].

References

[1] http://www.gammex.com/.

[2] C. Constantinou, F.H. Attix, and B.R. Paliwal. A solid water phantom material for radiotherapy x-ray and gamma-ray beam calibrations. *Med. Phys*, 1982.

[3] Slobodan Devic, Jan Seuntjens, Edwin Sham, Ervin B. Podgorsak, C. Ross Schmidtlein, Assen S. Kirov, and Christopher G. Soares. Precise radiochromic film dosimetry using a flat-bed document scanner. *Medical Physics*, 32(7):2245–2253, 2005.

[4] E. B. Podgorsak, editor. *Radiation Oncology Physics: A Handbook for Teachers and Students*. International Atomic Energy Agency, Vienna, 2005.

CHAPTER 4
Output Factor Measurements and Calculations

Contents

4.1 Methods

Several output factor measurements were taken to validate the CUTOUT code's output factor calculation performance. The measurements were performed in a Solid Water® phantom with pre-drilled openings for the ionization chamber. As mentioned earlier in this work, the depth of maximum dose for an electron beam will shift towards the surface of a phantom for small field sizes. Due to the limitations of the output factor measurement process, it is possible that the point of measurement is not at the true d_{max} as in the definition of an output factor. The MC measurements however, are determined at d_{max} since we aren't limited by practical concerns such as repeating a measurement several times to locate the shifted d_{max}, it is easily determined in the MC calculations.

The energies sampled for the cutout output factor measurements were 6, 9, 12, 16 and 20 MeV and for applicator sizes of 6×6 cm^2, 10×10 cm^2 and 15×15 cm^2. The cutouts were digitized in Cutout Manager where each job was created and submitted individually. Certain measurements are at extended SSD to ensure that cutouts with SSDs other than 100 cm could be calculated accurately as well. For some cases, the point of measurement was shifted laterally and longitudinally in both measurement and calculation. The calculations took about 2 hours each on one core of the Mac Pro (2.8 GHz CPU Core).

4.2 Results

The results of the measurement and MC calculation for each of the output factors evaluated are shown in tables 4–1 to 4–5 and are separated by energy. We note that the size of the image for each of the cases in tables 4–1 to 4–5 is equal to the applicator size. Most of the output factors measured were for 10×10 cm^2 cutouts since those are the most clinically prescribed cutout sizes. The calculations are in close agreement to the measurements with an overall mean percentage difference of 1.31% and mean calculation error of 1.56%. The greatest percentage difference observed was for a 6×6 cm^2 9 MeV cutout (case #1 in table 4–2). It is important to note that there is potential setup error in the measurements of the cutout output factors and that the points of measurement and calculation may be off by several mm. We estimate the error on a standard cutout output factor measurement to be $\approx 2\%$.

Cutout	Case	Cone (cm^2)	SSD (cm)	Meas. OF (%)	Calc. OF (%)	% Diff
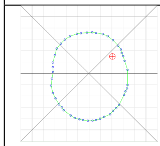	#1	10×10	100	93.5	94.7 ± 1.6	1.3%
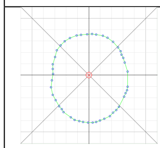	#2	10×10	100	100.3	100.8 ± 0.7	0.50%
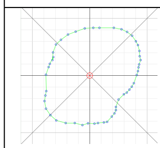	#3	10×10	100	100.6	98.8 ± 1.4	1.8%
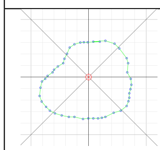	#4	10×10	100	100.2	101.2 ± 1.9	1.0
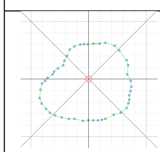	#5	10×10	105	88.9	89.7 ± 1.6	0.9%
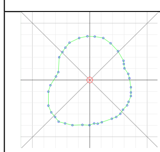	#6	10×10	100	100.3	99.4 ± 1.8	0.9%
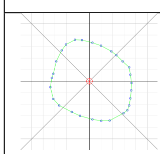	#7	10×10	100	100.5	100.4 ± 1.3	0.1%
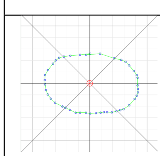	#8	10×10	100	100.3	99.3 ± 1.7	1.0%
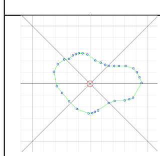	#9	10×10	100	99.9	100.1 ± 0.8	0.2%
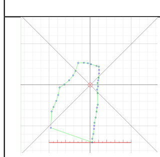	#10	15×15	100	100.2	99.0 ± 2.1	1.2%

Table 4–1: Percent difference between the output factor measurements and MC calculations for the 6 MeV beam.

Cutout	Case	Cone (cm^2)	SSD (cm)	Meas. OF (%)	Calc. OF (%)	% Diff
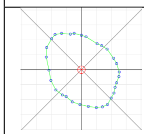	#1	6×6	101	94.7	91.6 ± 0.7	3.27%
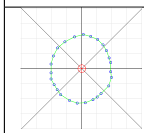	#2	6×6	100	95.1	93.4 ± 1.3	1.79%
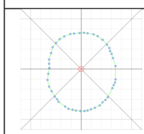	#3	10×10	100	100.1	98.8 ± 1.4	0.9%
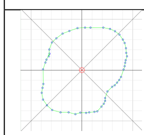	#4	10×10	100	100.3	101.1 ± 1.7	0.8%
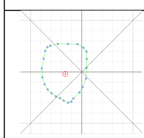	#5	10×10	102	93.7	92.5 ± 1.6	1.28%
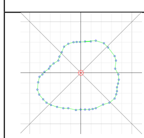	#6	10×10	100	100.0	98.4 ± 1.6	1.6%
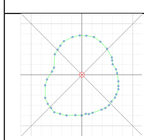	#7	10×10	100	100.2	98.9 ± 1.9	1.3%
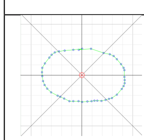	#8	10×10	100	99.7	101.9 ± 1.8	2.21%
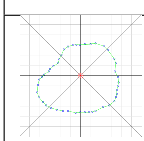	#9	10×10	100	98.8	95.7 ± 0.4	3.14%
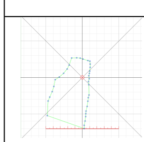	#10	15×15	101	98.2	98.5 ± 2.2	0.31%
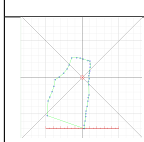	#11	15×15	100	100.7	98.5 ± 2.2	0.31%

Table 4–2: Percent difference between the output factor measurements and MC calculations for the 9 MeV beam.

Cutout	Case	Cone (cm^2)	SSD (cm)	Meas. OF (%)	Calc. OF (%)	% Diff
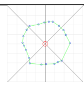	#1	6×6	100	95.5	94.2 ± 0.7	1.36%
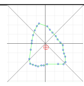	#2	6×6	100	93.0	92.3 ± 0.6	0.75%
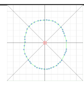	#3	10×10	100	99.8	102.4 ± 1.9	2.61%
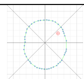	#4	10×10	100	91.3	91.0 ± 1.9	0.33%
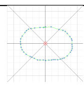	#5	10×10	100	99.1	96.9 ± 0.9	2.22%
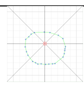	#6	10×10	100	98.3	97.5 ± 1.7	0.81%
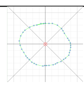	#7	10×10	100	100.0	97.9 ± 0.8	2.10%
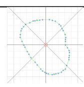	#8	10×10	100	100.1	101.4 ± 2.0	1.30%
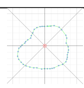	#9	10×10	100	99.6	100.5 ± 1.9	0.90%
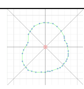	#10	10×10	100	99.9	99.0 ± 1.8	0.90%
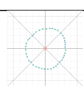	#11	10×10	100	99.5	98.7 ± 1.9	0.80%
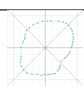	#12	10×10	100	100.0	99.2 ± 2.0	0.80%
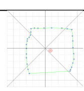	#13	10×10	101.5	97.2	96.5 ± 1.8	0.72%
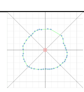	#14	10×10	100	99.6	100.0 ± 1.7	0.40%
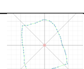	#15	15×15	100	100.3	98.6 ± 2.2	1.69%
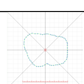	#16	15×15	100	100.1	98.4 ± 1.1	1.70%

Table 4–3: Percent difference between the output factor measurements and MC calculations for the 12 MeV beam.

Cutout	Case	Cone (cm^2)	SSD (cm)	Meas. OF (%)	Calc. OF (%)	% Diff
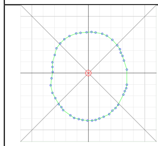	#1	10×10	100	99.8	98.6 ± 1.6	1.2%
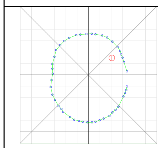	#2	10×10	100	95.2	95.6 ± 2.2	0.42%
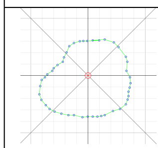	#3	10×10	100	99.8	100.9 ± 2.0	1.1%
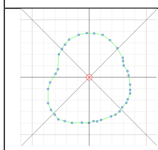	#4	10×10	100	100.0	96.9 ± 1	3.10%
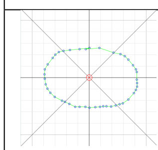	#5	10×10	100	99.6	98.6 ± 0.9	1.0%
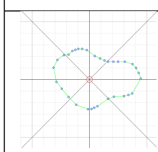	#6	10×10	100	99.2	96.7 ± 0.9	2.52%
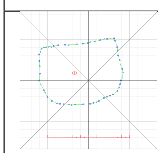	#7	15×15	100	100.2	98.0 ± 2.3	2.20%
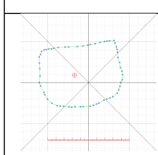	#8	15×15	105	89.9	91.6 ± 2.4	1.89%

Table 4–4: Percent difference between the output factor measurements and MC calculations for the 16 MeV beam.

Cutout	Case	Cone (cm^2)	SSD (cm)	Meas. OF (%)	Calc. OF (%)	% Diff
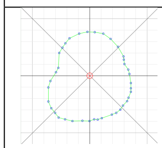	#1	10×10	100.2	99.8	100.9 ± 2.3	0.7%

Table 4–5: Percent difference between the output factor measurements and MC calculations for the 20 MeV beam.

CHAPTER 5
Profile Verification of Electron Beam Monte Carlo Calculations

Contents

5.1 Methods

Two custom designed cutouts were created to evaluate the performance of the electron beam MC calculation engine. The first cutout to be studied is for the 10×10 cm^2 applicator and is in the shape of a triangle and thus will be referred to as the triangle cutout. The cutout is shown in figure 5–1a and has dimensions of 5.5 cm for each side.

The second cutout studied is in the shape of a bow tie and fits a 15×15 cm^2 electron applicator. The cutout is shown in figure 5–1b and has dimensions of 5 cm for the short side and 10 cm for the long side. It was designed in such a fashion as to give full electron lateral scatter contribution for lower energies and less for larger energies to investigate whether or not the MC calculations could accurately calculate dose in such a situation.

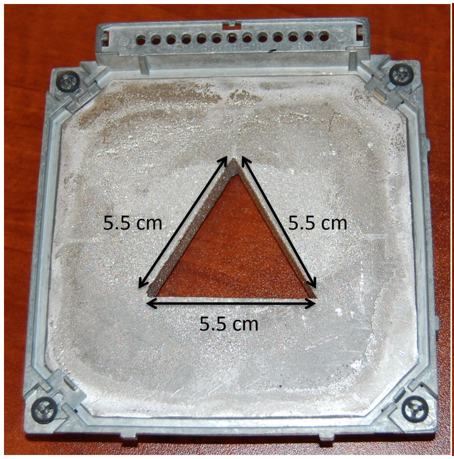

(a) Triangle cutout for the 10×10 cm^2 applicator.

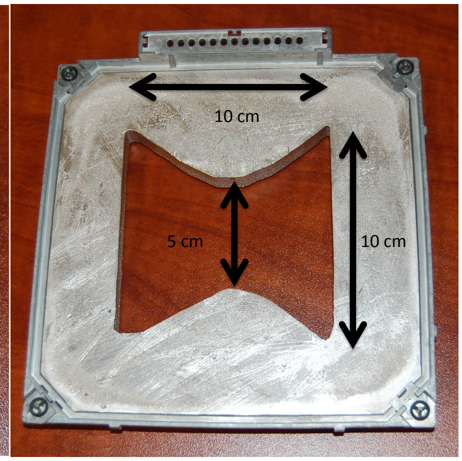

(b) Bow tie cutout for the 15×15 cm^2 applicator.

Figure 5–1: Custom designed cutouts used for profile measurement and MC calculation comparisons.

For each cutout, profiles were measured in water using the Blue Phantom for energies of 6, 9, 12, 16 and 20 MeV in both the "X" and "Y" orientations (as defined in figures 5–2 and 5–8) and at the depths of $z_{\max}$ and the approximative R_{50}. The measurements were taken on the JGH's Varian Clinac iX linear accelerator. The actual depths of measurement for the profiles are listed in table 5–1.

	Triangle		Bow tie	
Energy	$Z_{\max}$	R_{50}	$Z_{\max}$	R_{50}
6 MeV	1.5 cm	2.4 cm	1.4 cm	2.3 cm
9 MeV	2.1 cm	3.6 cm	2.2 cm	3.6 cm
12 MeV	2.7 cm	4.8 cm	2.9 cm	5.0 cm
16 MeV	2.7 cm	6.6 cm	3.2 cm	6.6 cm
20 MeV	1.8 cm	8.1 cm	1.9 cm	8.5 cm

Table 5–1: Measured values for $z_{\max}$ and R_{50} for each of the energies used for the comparison.

The measurements were acquired using a Wellhöfer CC13 ionization chamber and OmniPro software was used to export the profiles to ASCII format.The MC calculations were performed in MMCTP and the profiles were extracted at the desired depths and exported into an ASCII file. Each pair of measurement and calculation data set was imported into MATLAB where the results were displayed. The results were normalized to the maximum value of the profile and a shift was applied for proper profile overlap. Note that the shift was up to a maximum of 4 mm. The reason for the shift is that there is a level of uncertainty in the setup, whereby the location of the profile may or may not be exactly in the centre of the cutout. Thus for proper comparison it proved necessary to shift either of the profiles to align them.

5.2 Profile Comparison of the Triangle Shaped Cutout

Profiles were measured for the triangle cutout for each of the electron energies in both the “X” and ‘Y” orientation, where they are defined in figure 5–2. The comparison of the measured and calculated profiles are shown in figures 5–3 to 5–7 with percentage error superimposed on each plot in the central portion of the field. The percentage error was calculated as follows:

$$\% \text{ Error} = 100 \times \frac{\text{(Calculated-Measured)}}{\text{Measured}} \tag{5.1}$$

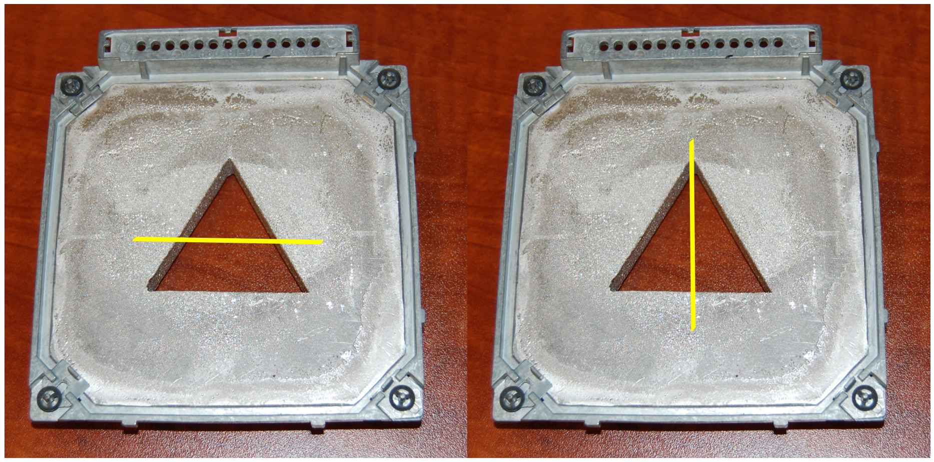

(a) "X" orientation of profile. (b) "Y" orientation of profile.

Figure 5–2: Custom made triangular shaped cutout used for profile measurements and MC calculations. For the purpose of this work, the "X" orientation of the profile is that which was measured and calculated along the line shown in (a) and the "Y" is seen in (b).

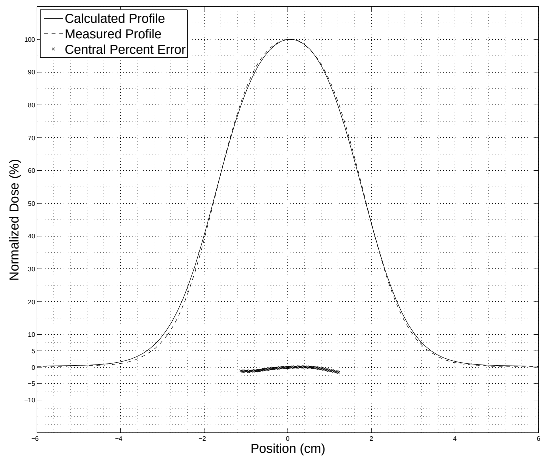

(a) 6 MeV profile with "X" orientation at a depth of 1.5 cm.

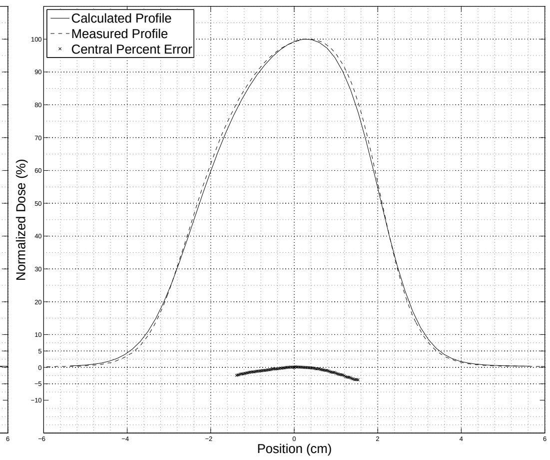

(b) 6 MeV profile with "Y" orientation at a depth of 1.5 cm.

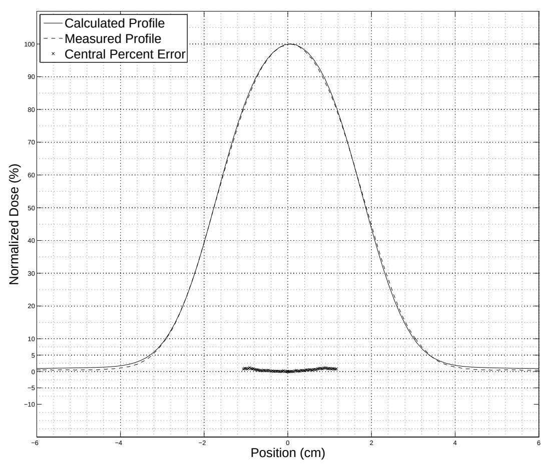

(c) 6 MeV profile with "X" orientation at a depth of 2.4 cm.

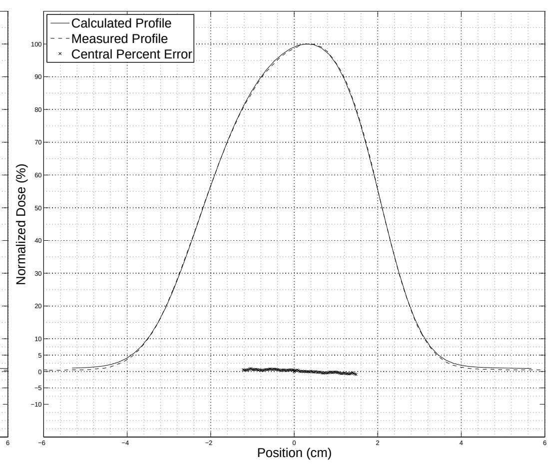

(d) 6 MeV profile with "Y" orientation at a depth of 2.4 cm.

Figure 5–3: Profile comparisons of a measured 6 MeV electron beam vs MC calculated beam within water. The triangular shaped cutout was used and the depth of measurement and calculation was 1.5 cm in (a) and (b) and 2.4 cm in (c) and (d).

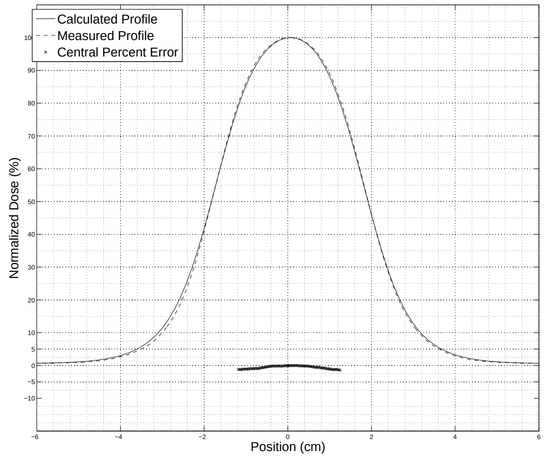

(a) 9 MeV profile with "X" orientation at a depth of 2.1 cm.

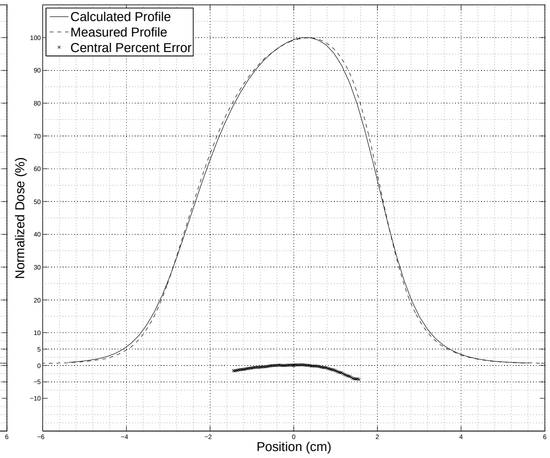

(b) 9 MeV profile with "Y" orientation at a depth of 2.1 cm.

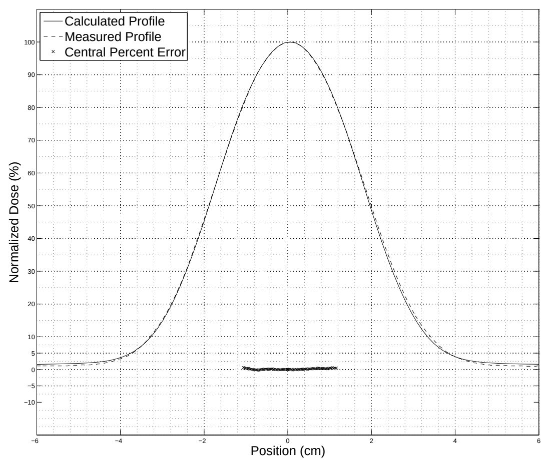

(c) 9 MeV profile with "X" orientation at a depth of 3.6 cm.

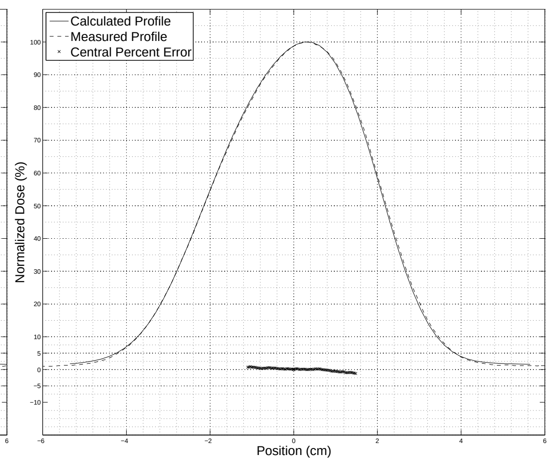

(d) 9 MeV profile with "Y" orientation at a depth of 3.6 cm.

Figure 5–4: Profile comparisons of a measured 9 MeV electron beam vs MC calculated beam within water. The triangular shaped cutout was used and the depth of measurement and calculation was 2.1 cm in (a) and (b) and 3.6 cm in (c) and (d).

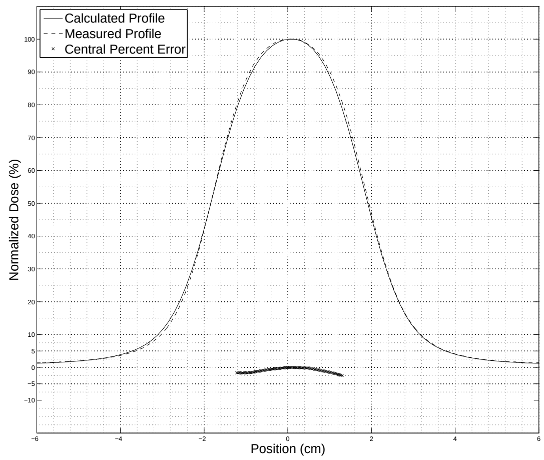

(a) 12 MeV profile with "X" orientation at a depth of 2.7 cm.

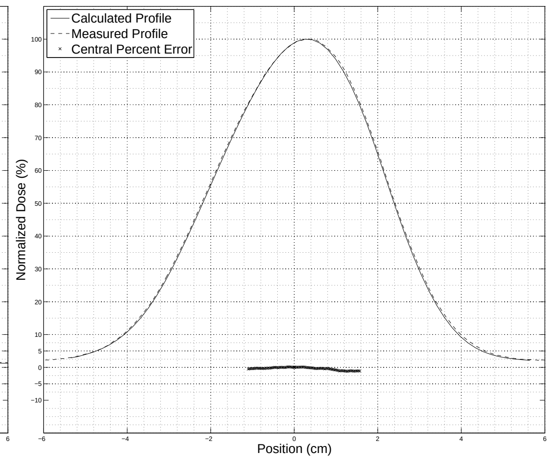

(b) 12 MeV profile with "Y" orientation at a depth of 2.7 cm.

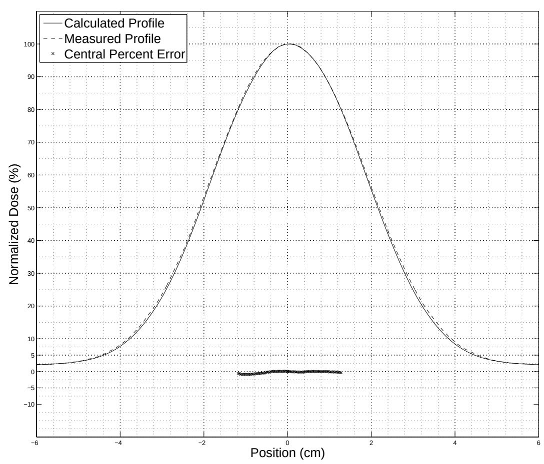

(c) 12 MeV profile with "X" orientation at a depth of 4.8 cm.

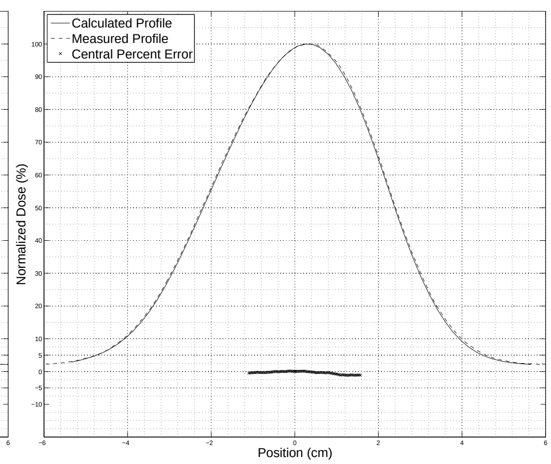

(d) 12 MeV profile with "Y" orientation at a depth of 4.8 cm.

Figure 5–5: Profile comparisons of a measured 12 MeV electron beam vs MC calculated beam within water. The triangular shaped cutout was used and the depth of measurement and calculation was 2.7 cm in (a) and (b) and 4.8 cm in (c) and (d).

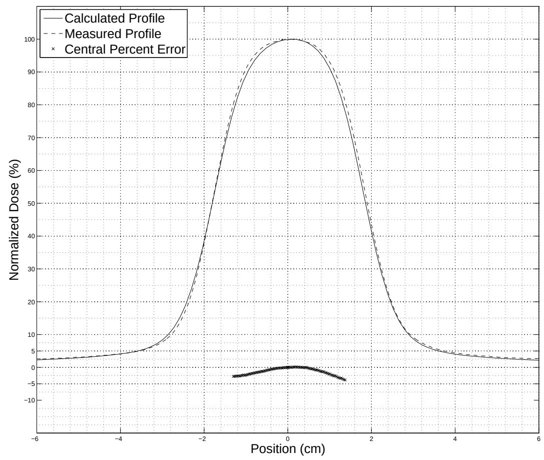

(a) 16 MeV profile with "X" orientation at a depth of 2.7 cm.

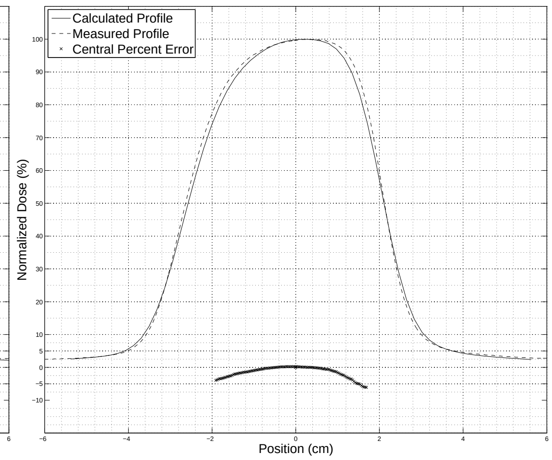

(b) 16 MeV profile with "Y" orientation at a depth of 2.7 cm.

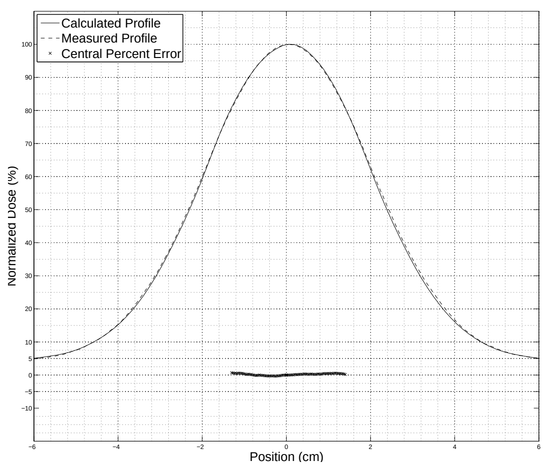

(c) 16 MeV profile with "X" orientation at a depth of 6.6 cm.

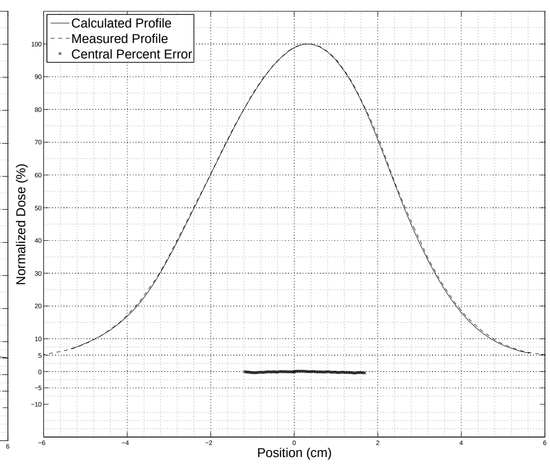

(d) 16 MeV profile with "Y" orientation at a depth of 6.6 cm.

Figure 5–6: Profile comparisons of a measured 16 MeV electron beam vs MC calculated beam within water. The triangular shaped cutout was used and the depth of measurement and calculation was 2.7 cm in (a) and (b) and 6.6 cm in (c) and (d).

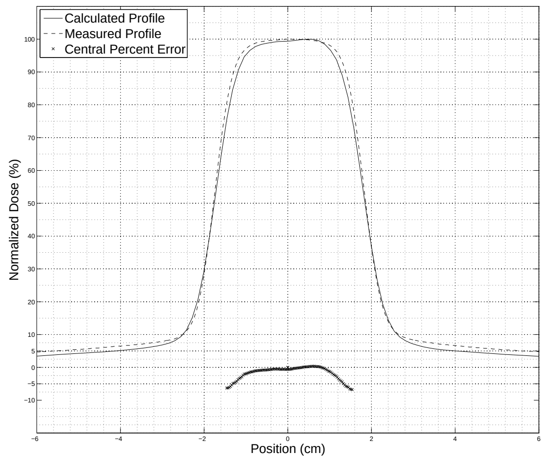

(a) 20 MeV profile with “X” orientation at a depth of 1.8 cm.

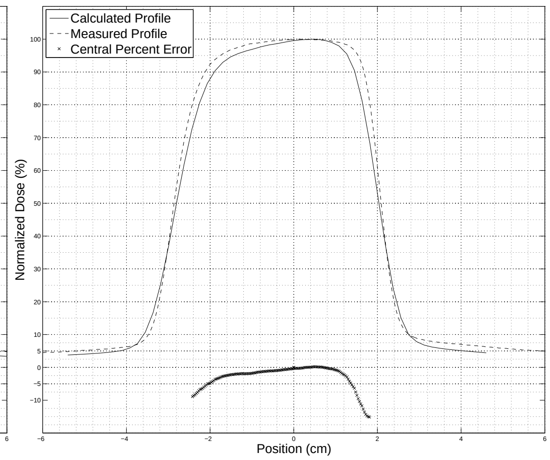

(b) 20 MeV profile with “Y” orientation at a depth of 1.8 cm.

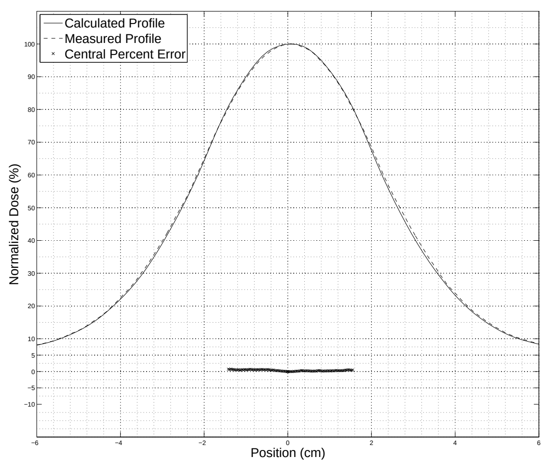

(c) 20 MeV profile with “X” orientation at a depth of 8.1 cm.

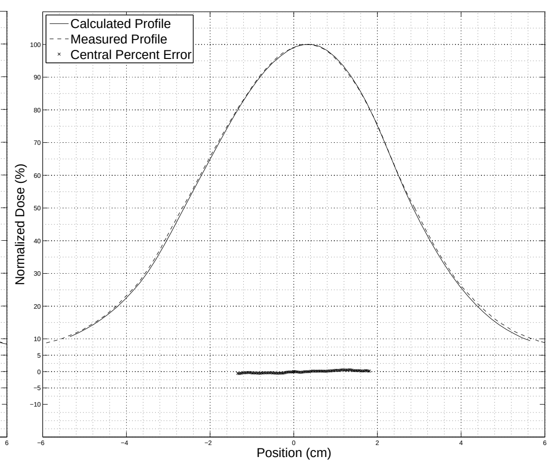

(d) 20 MeV profile with “Y” orientation at a depth of 8.1 cm.

Figure 5–7: Profile comparisons of a measured 20 MeV electron beam vs MC calculated beam within water. The triangular shaped cutout was used and the depth of measurement and calculation was 1.8 cm in (a) and (b) and 8.1 cm in (c) and (d).

An important feature to note is that the X profiles are quite symmetric about the origin but the Y profiles seem to be skewed to the right. This is due to the fact that the triangle cutout opening gets larger along the profile; this means that there will be more scatter and thus a higher dose near the side of the triangle with the larger opening. This phenomenon is what can be seen in all of the Y profiles in the figures above.

The MC agrees quite well with the measurements, especially for the lower energies up until 20 MeV where larger discrepancies are seen. The largest discrepancy is in figure 5–7b for the 20 MeV Y profile at the depth of 1.8 cm where the error approaches 15%. However for the same energy at the deeper depth of 8.1 cm (figure 5–7d) there is much better agreement. A theory which will account for this will have to have several features. The trend seems to increase with increasing energy and the discrepancy decreases with depth for a given profile. For this reason, we can conclude that it is not due to an offset in the plane of measurement because any offset would be enhanced at R_{50} since the PDD slope is steeper there, yet it decreases at depth. So a possible theory would be that for the small triangle cutout there might be increased scatter that the MC doesn't pick up and these scattered electrons get absorbed before reaching R_{50} and thus will not show up in the measurements, yielding good correlation with the MC. The reason that it increases with energy is most likely because the scattered secondary electrons have greater energy thus depositing more dose.

Overall however, there seems to be good correlation between the measured and MC calculated profiles for the triangle cutout especially for energies below 20 MeV which are the clinically relevant energies for electron beams anyway.

5.3 Profile Comparison of the Bow Tie Shaped Cutout

The bow tie cutout profiles have undergone the same treatment and their results are displayed in figures 5–9 to 5–13.

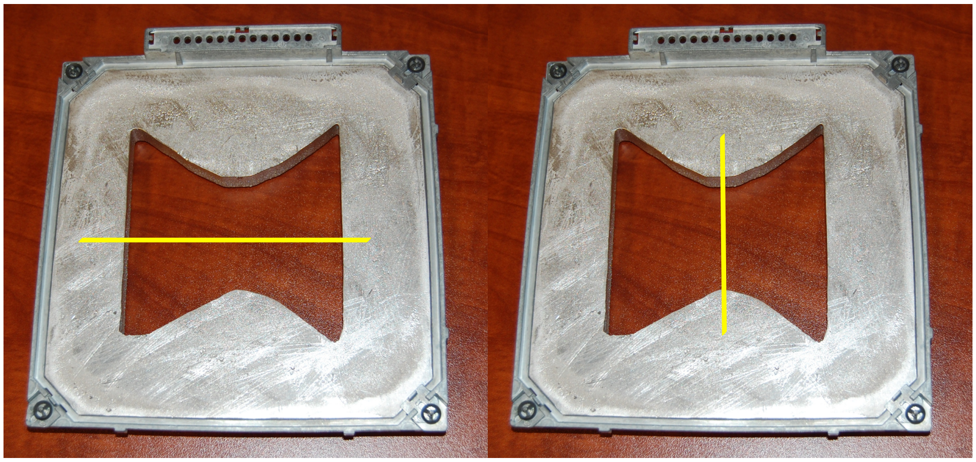

(a) "X" orientation of profile.　　(b) "Y" orientation of profile.

Figure 5–8: Custom made bow tie shaped cutout used for profile measurements and MC calculations. For the purpose of this work, the "X" orientation of the profile is that which was measured and calculated along the line shown in (a) and the "Y" is seen in (b).

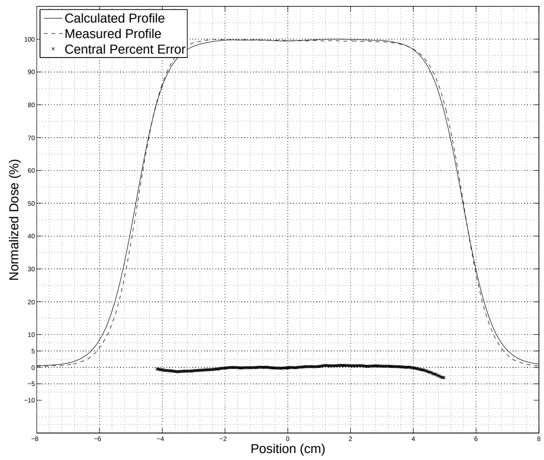

(a) 6 MeV profile with “X” orientation at a depth of 1.4 cm.

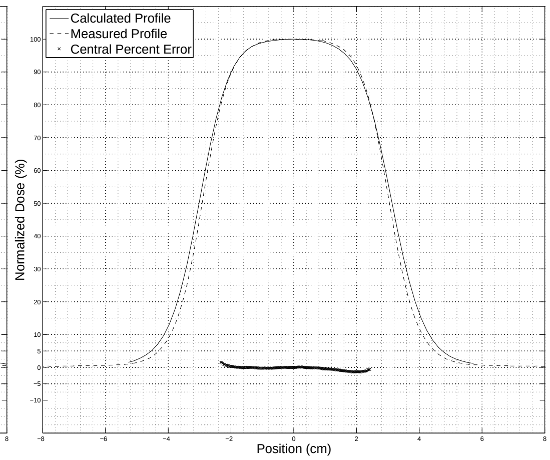

(b) 6 MeV profile with “Y” orientation at a depth of 1.4 cm.

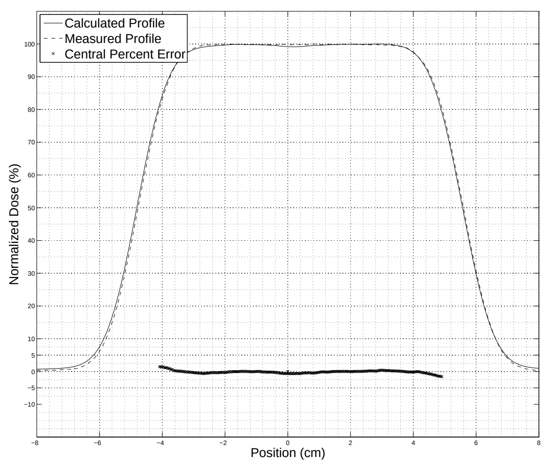

(c) 6 MeV profile with “X” orientation at a depth of 2.3 cm.

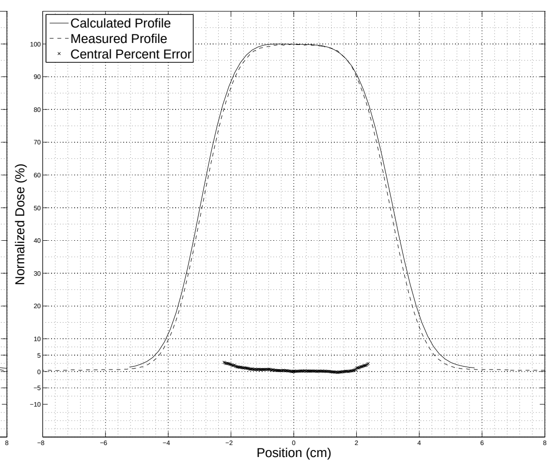

(d) 6 MeV profile with “Y” orientation at a depth of 2.3 cm.

Figure 5–9: Profile comparisons of a measured 6 MeV electron beam vs MC calculated beam within water. The bow tie shaped cutout was used and the depth of measurement and calculation was 1.4 cm in (a) and (b) and 2.3 cm in (c) and (d).

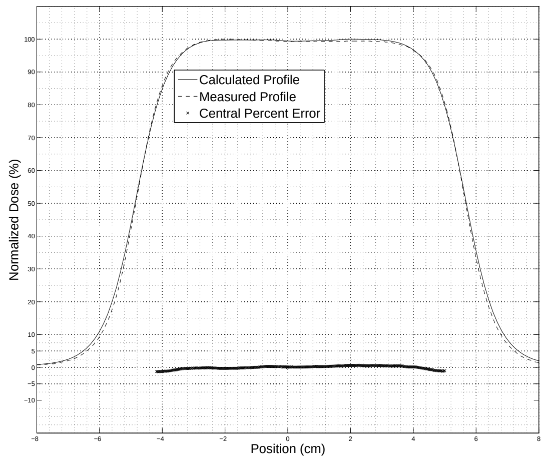

(a) 9 MeV profile with “X” orientation at a depth of 2.2 cm.

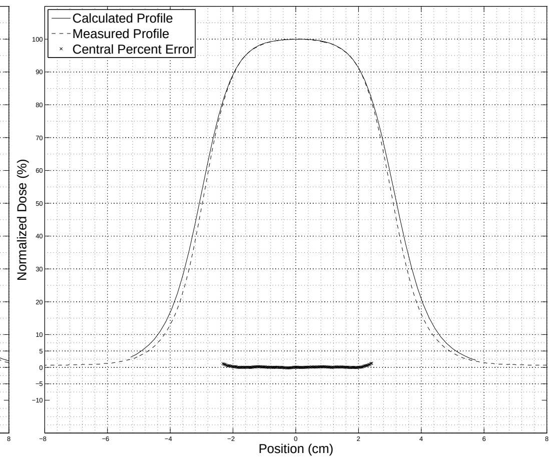

(b) 9 MeV profile with “Y” orientation at a depth of 2.2 cm.

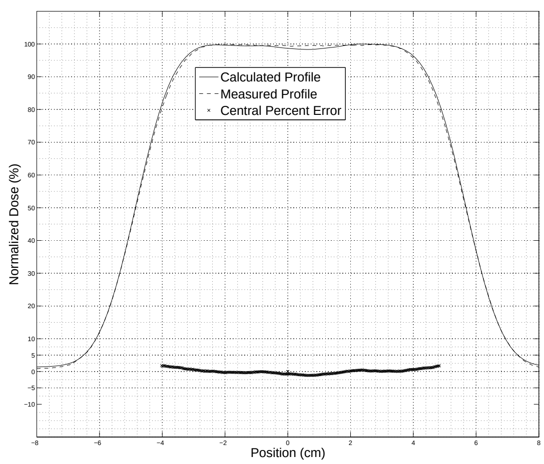

(c) 9 MeV profile with “X” orientation at a depth of 3.6 cm.

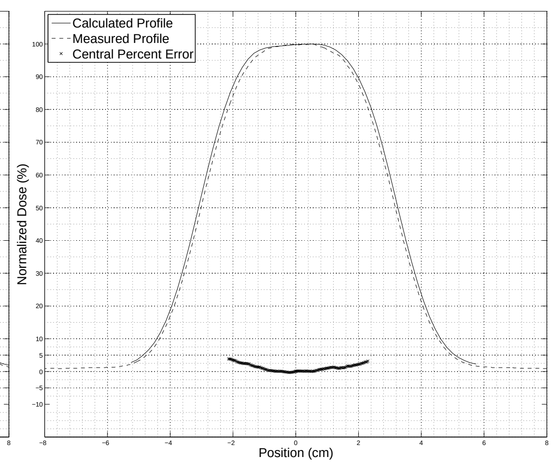

(d) 9 MeV profile with “Y” orientation at a depth of 3.6 cm.

Figure 5–10: Profile comparisons of a measured 9 MeV electron beam vs MC calculated beam within water. The bow tie shaped cutout was used and the depth of measurement and calculation was 2.2 cm in (a) and (b) and 3.6 cm in (c) and (d).

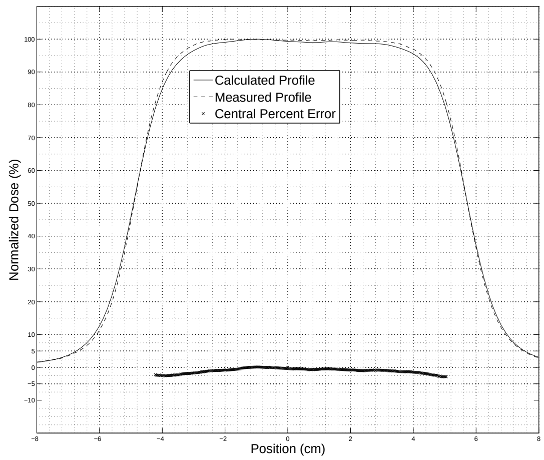

(a) 12 MeV profile with “X” orientation at a depth of 2.9 cm.

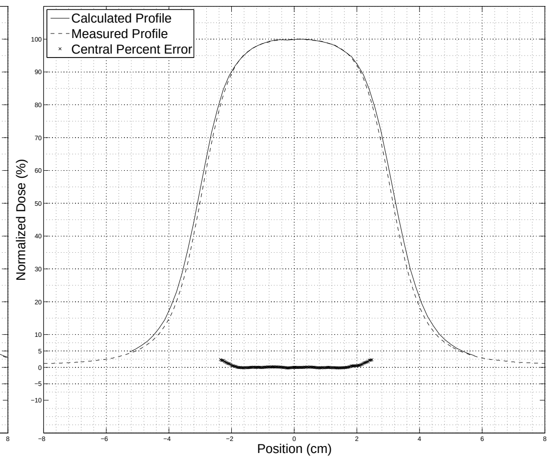

(b) 12 MeV profile with “Y” orientation at a depth of 2.9 cm.

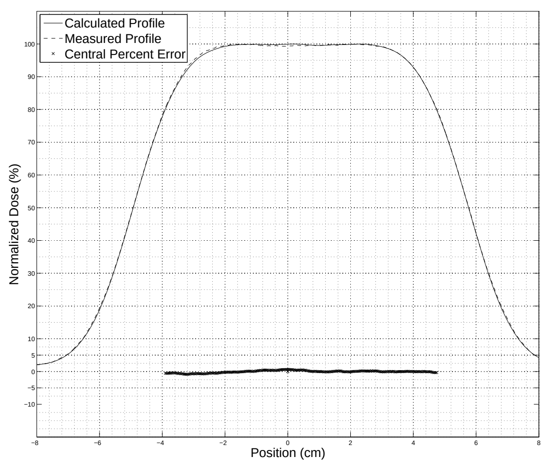

(c) 12 MeV profile with “X” orientation at a depth of 5.0 cm.

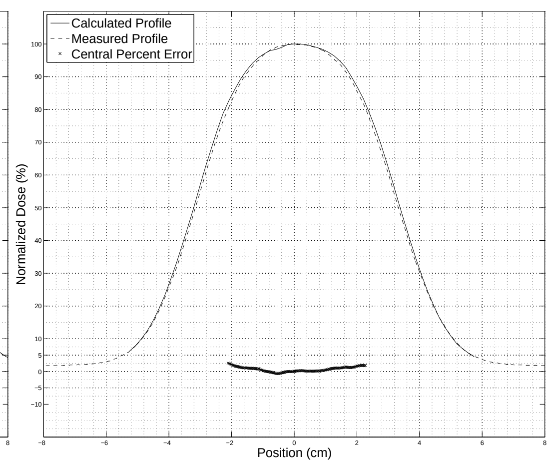

(d) 12 MeV profile with “Y” orientation at a depth of 5.0 cm.

Figure 5–11: Profile comparisons of a measured 12 MeV electron beam vs MC calculated beam within water. The bow tie shaped cutout was used and the depth of measurement and calculation was 2.9 cm in (a) and (b) and 5.0 cm in (c) and (d).

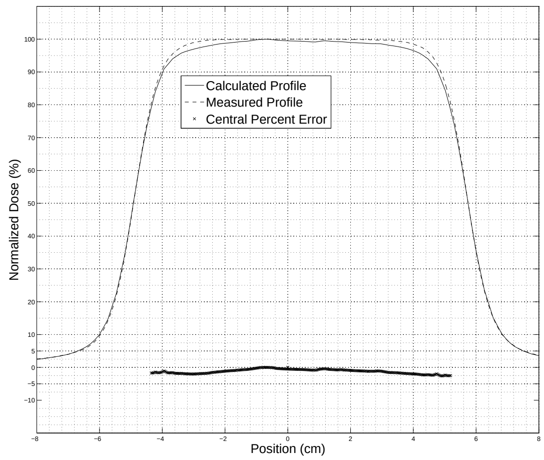

(a) 16 MeV profile with "X" orientation at a depth of 3.2 cm.

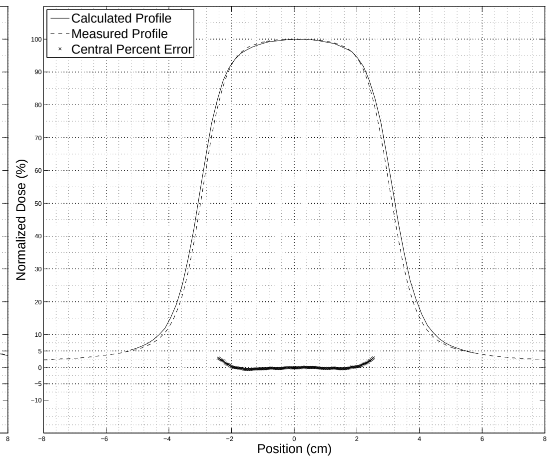

(b) 16 MeV profile with "Y" orientation at a depth of 3.2 cm.

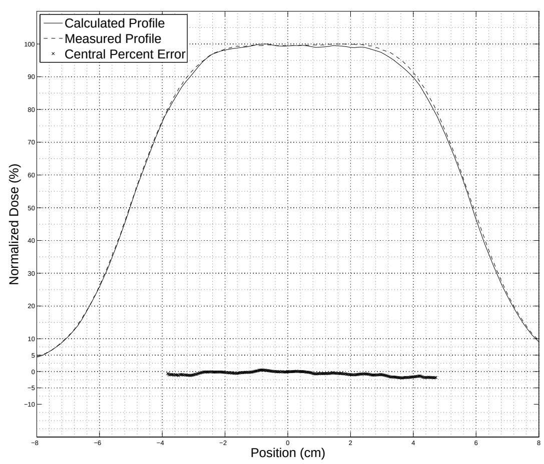

(c) 16 MeV profile with "X" orientation at a depth of 6.6 cm.

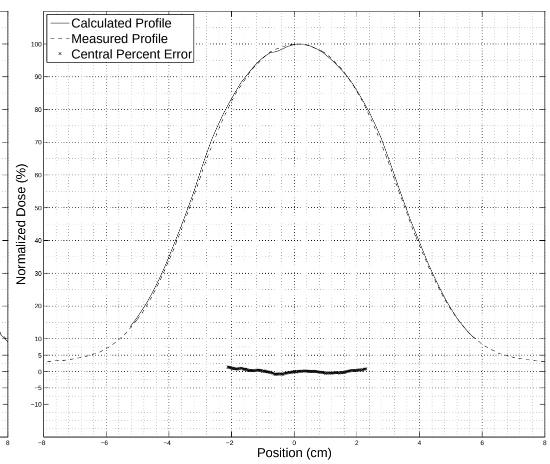

(d) 16 MeV profile with "Y" orientation at a depth of 6.6 cm.

Figure 5–12: Profile comparisons of a measured 16 MeV electron beam vs MC calculated beam within water. The bow tie shaped cutout was used and the depth of measurement and calculation was 3.2 cm in (a) and (b) and 6.6 cm in (c) and (d).

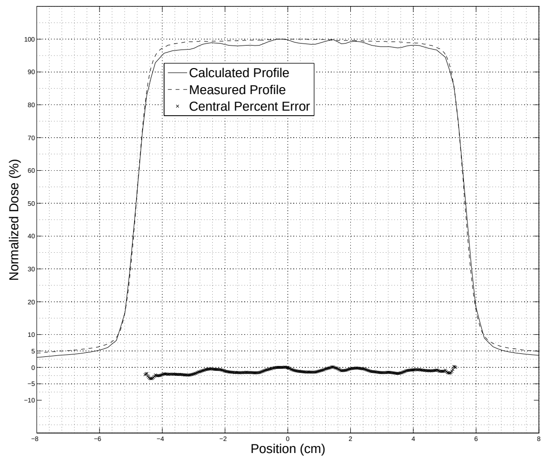

(a) 20 MeV profile with "X" orientation at a depth of 1.9 cm.

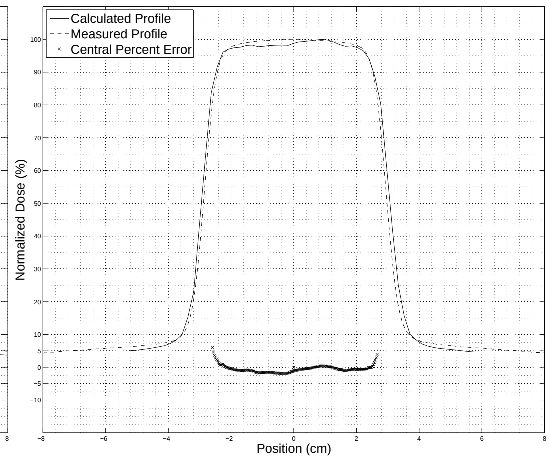

(b) 20 MeV profile with "Y" orientation at a depth of 1.9 cm.

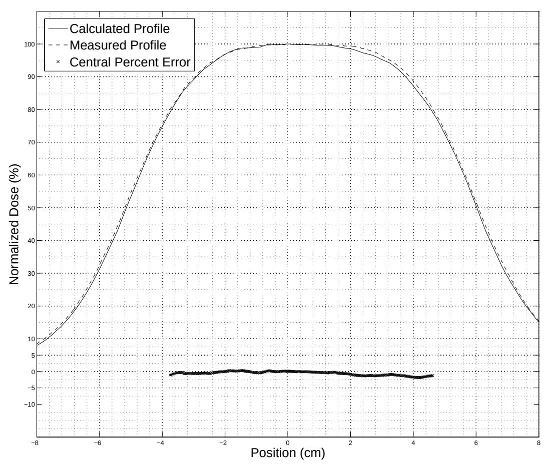

(c) 20 MeV profile with "X" orientation at a depth of 8.5 cm.

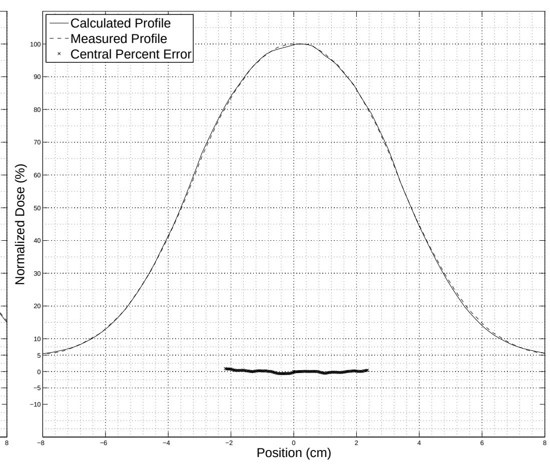

(d) 20 MeV profile with "Y" orientation at a depth of 8.5 cm.

Figure 5–13: Profile comparisons of a measured 20 MeV electron beam vs MC calculated beam within water. The bow tie shaped cutout was used and the depth of measurement and calculation was 1.9 cm in (a) and (b) and 8.5 cm in (c) and (d).

The bow tie cutout results are quite good with an upper limit on the error around 2.5%. A strange phenemenon can be observed in the 20 MeV case at the depth of 1.9 cm both in the X and Y orientations (see figures 5–13a and 5–13b). The profiles show a wavy pattern with an error of about 2% relative to measurements. The problem seems to be ameliorated at the greater depth of 8.5 cm for the same energy (figures 5–13c and 5–13d).

CHAPTER 6
Heterogeneous Electron Beam Film Measurements and MC Calculations

Contents

6.1 Methods

To evaluate the heterogeneous performance of the electron MC system, two heterogeneous phantoms were acquired from G. Kamta's Master's thesis work at McGill University [1]. The first phantom is made of Solid Water® with two embedded lung tissue equivalent rods and is pictured in figure 6–1a. The second phantom consists of a slab of Solid Water® with three Bone equivalent rods superimposed (figure 6–1b).

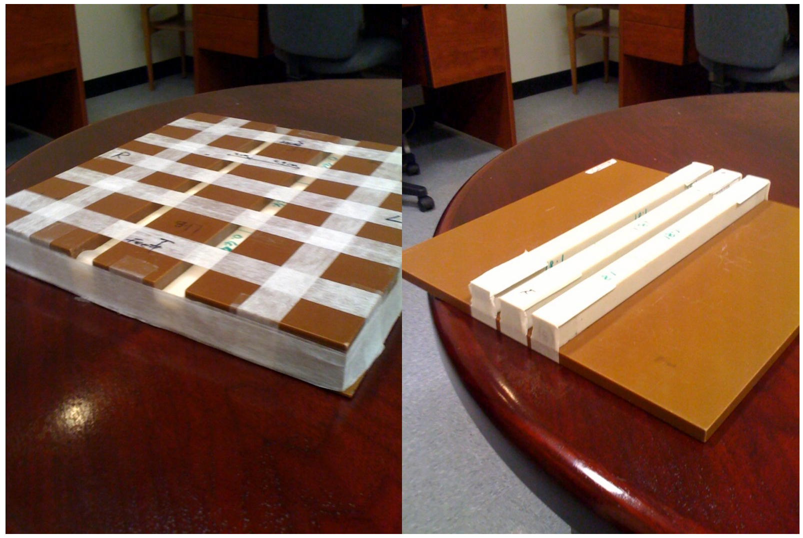

(a) Lung (b) Bone

Figure 6–1: Heterogenous phantoms used to evaluate the electron MC heterogenous performance

Once acquired, the phantoms were CT scanned and imported into MMCTP. MMCTP converts the CT data into a virtual phantom called an EGSphant file. The resolution of the phantom is 3 mm by 3 mm in the x and y planes. A 15×15 cm^2 applicator was used with the standard cutout. The MC calculation was performed within MMCTP by first generating the phase-space file at the base of the cutout and then using that file to generate the phantom dose map using DOSXYZnrc. This was done for each available electron energy: 6, 9, 12 ,16 and 20 MeV. The measurements were performed using EBT2 Gafchromic film. The films were placed at the base of each phantom, at a depth of approximately 3 cm and a film was irradiated for each energy. The depth of measurement was fixed and did not change with energy. Once the MC calculations were completed, each dose distribution was exported as an RT dose plan and imported into FilmQA for comparison with the film measurements. Profiles and gamma comparisons were used with criteria of 3% for dose difference and 3 mm for distance-to-agreement for the gamma.

6.2 Results

Figures 6–2 to 6–6 show the gamma and profile comparisons for the lung phantom and figures 6–7 to 6–11 are for the bone phantom.

6.2.1 Lung Tissue Phantom

The region of interest (ROI) for the gamma comparisons were selected to be the centre of the phantom and the histogram statistics are confined to the ROI. The following figures contain the gamma comparison with histogram and profiles for each of the energies used.

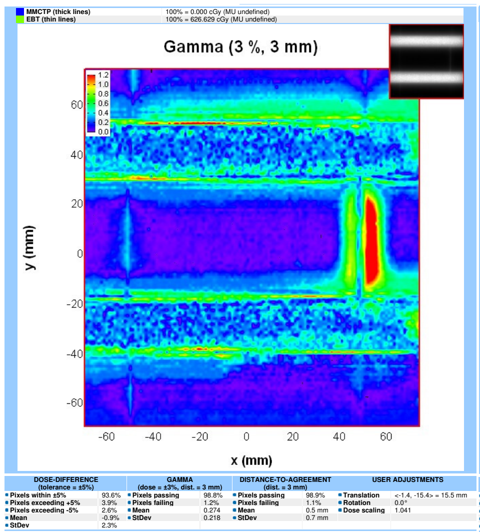

(a) Gamma comparison between MC calculations and film measurements for 6 MeV electrons in the lung phantom.

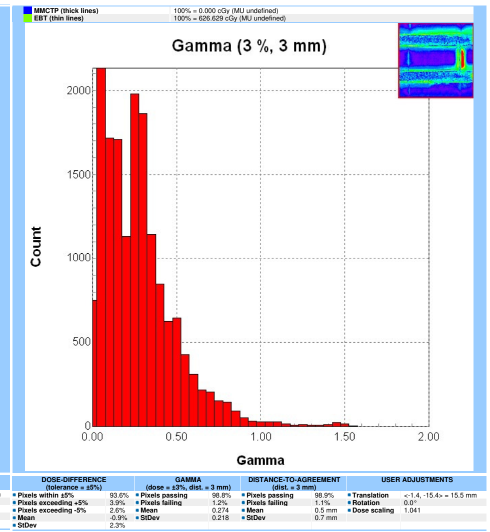

(b) Histogram of the gamma map in 6–2a.

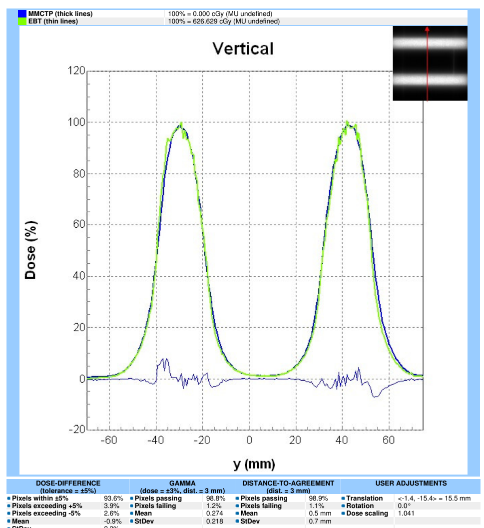

(c) Profile comparison between MC and film measurements for 6 MeV electrons in the lung phantom.

Figure 6–2: Comparison of MC calculation and film measurements for a 15×15 cm^2 6 MeV electron beam in the lung phantom.

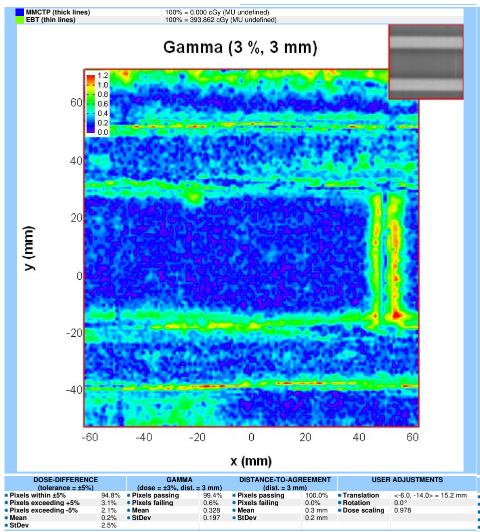

(a) Gamma comparison between MC calculations and film measurements for 9 MeV electrons in the lung phantom.

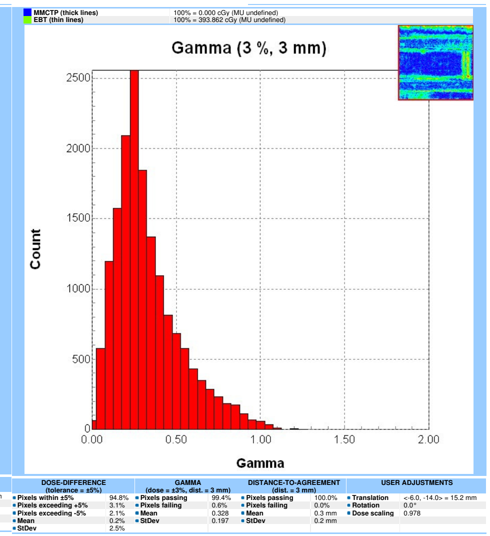

(b) Histogram of the gamma map in 6–3a.

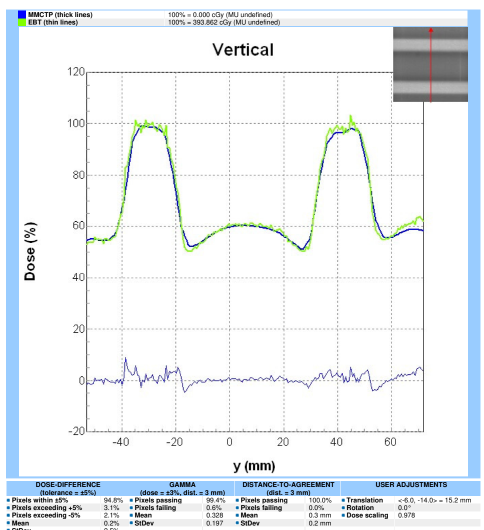

(c) Profile comparison between MC and film measurements for 9 MeV electrons in the lung phantom.

Figure 6–3: Comparison of MC calculation and film measurements for a 15×15 cm^2 9 MeV electron beam in the lung phantom.

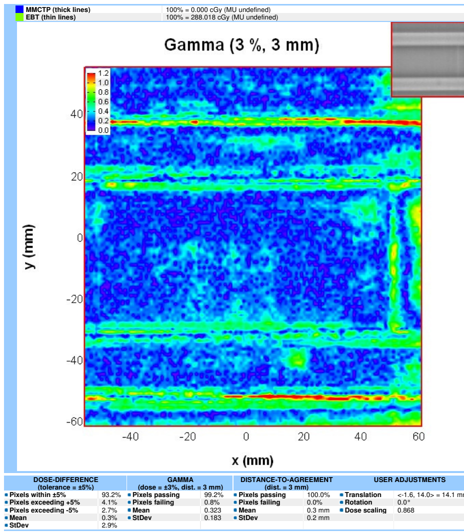

(a) Gamma comparison between MC calculations and film measurements for 12 MeV electrons in the lung phantom.

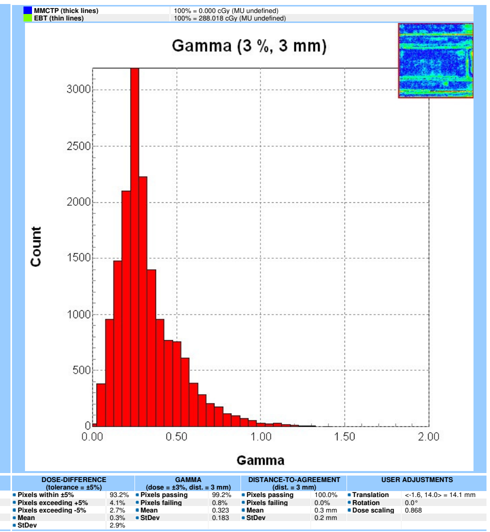

(b) Histogram of the gamma map in 6–4a.

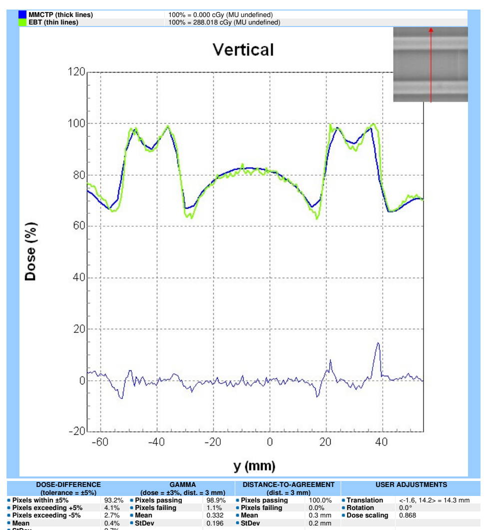

(c) Profile comparison between MC and film measurements for 12 MeV electrons in the lung phantom.

Figure 6–4: Comparison of MC calculation and film measurements for a 15×15 cm^2 12 MeV electron beam in the lung phantom.

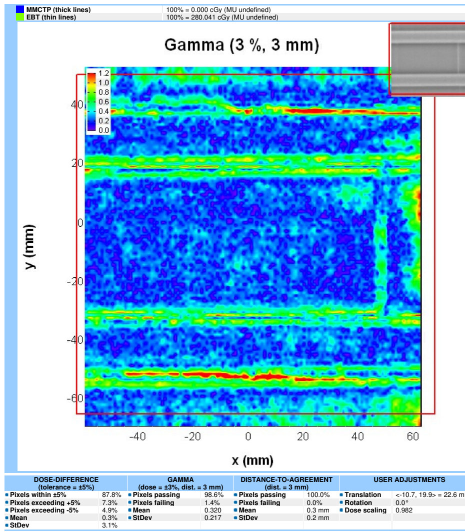

(a) Gamma comparison between MC calculations and film measurements for 16 MeV electrons in the lung phantom.

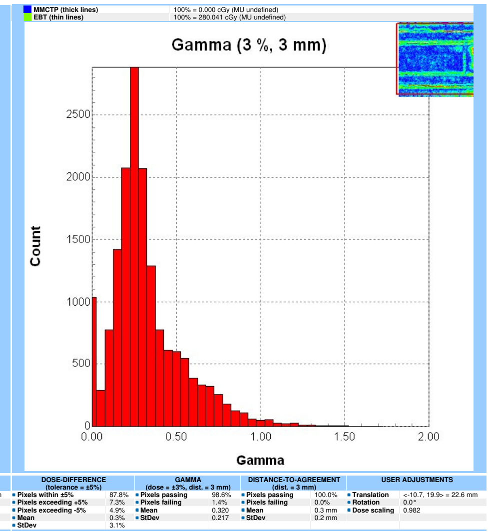

(b) Histogram of the gamma map in 6–5a.

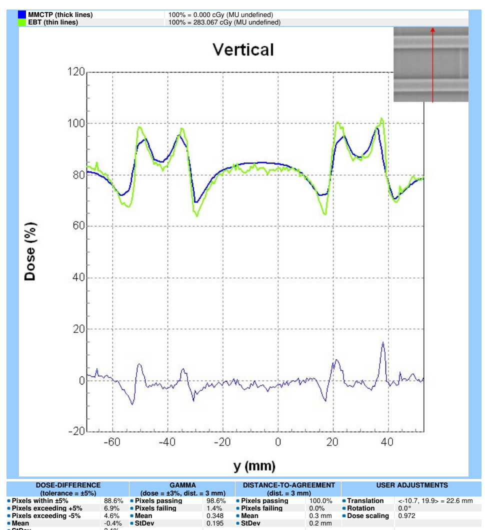

(c) Profile comparison between MC and film measurements for 16 MeV electrons in the lung phantom.

Figure 6–5: Comparison of MC calculation and film measurements for a 15×15 cm^2 16 MeV electron beam in the lung phantom.

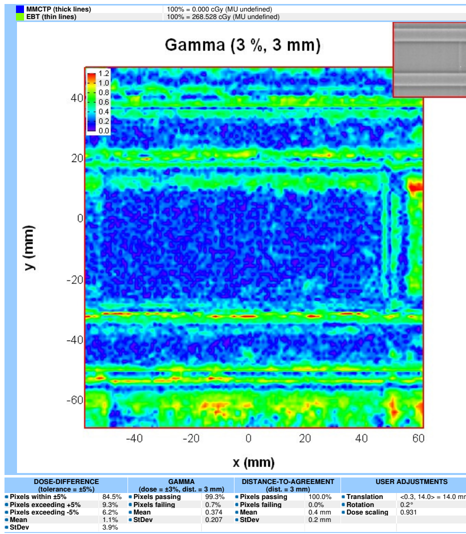

(a) Gamma comparison between MC calculations and film measurements for 20 MeV electrons in the lung phantom.

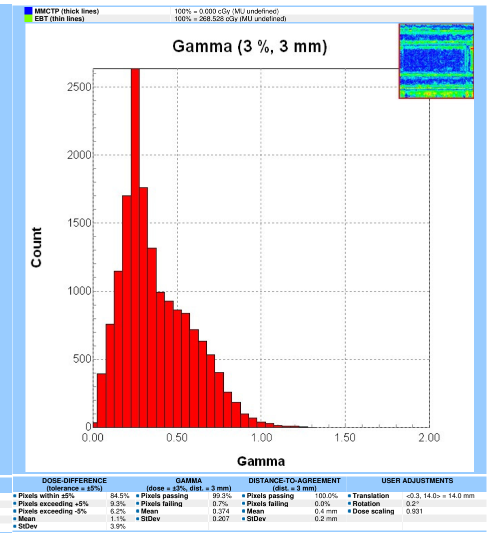

(b) Histogram of the gamma map in 6–5a.

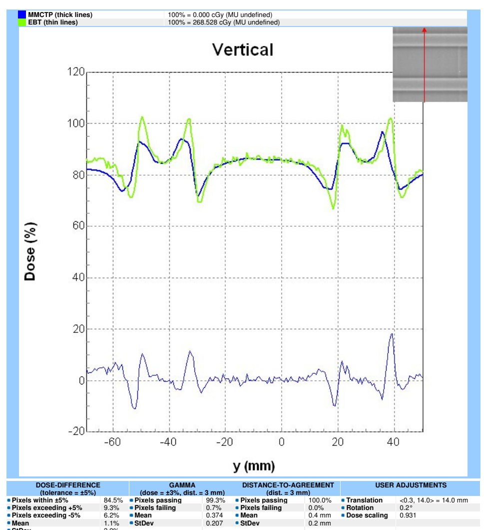

(c) Profile comparison between MC and film measurements for 20 MeV electrons in the lung phantom.

Figure 6–6: Comparison of MC calculation and film measurements for a 15×15 cm^2 20 MeV electron beam in the lung phantom.

The lung phantom has a small air gap in the Solid Water® slabs which was used to aid positioning and orientation. The gamma maps show an area of discrepancy over this gap and decreases with increasing energy (see figure 6–2a for example). The discrepancy is due to the higher amount of electron scatter in lower energies.

The gamma comparisons show that the measurements and MC calculations are in close agreement with $> 98.6\%$ of the pixels passing within the ROI used. Table 6–1 lists the percent of pixels passing the gamma comparison for each energy. It is also worthy to note the spikes in the profile for the higher energies (see figure 6–6c). This is due to the scattering of the electrons off the Solid Water® near the lung interface and is more apparent for higher energies.

Energy (MeV)	Percentage of Pixels Passing
6	98.8%
9	99.4%
12	99.2%
16	98.6%
20	99.3%

Table 6–1: Percentage of pixels passing within the ROI used for the gamma comparison of the film measurements and MC calculated dose distribution in the lung phantom.

6.2.2 Bone Tissue Phantom

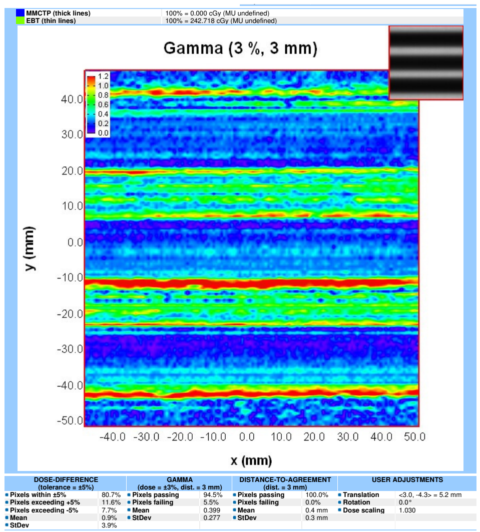

(a) Gamma comparison between MC calculations and film measurements for 6 MeV electrons in the bone phantom.

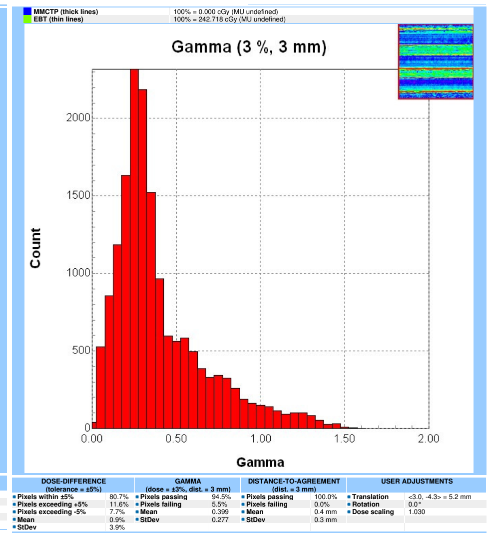

(b) Histogram of the gamma map in 6–7a.

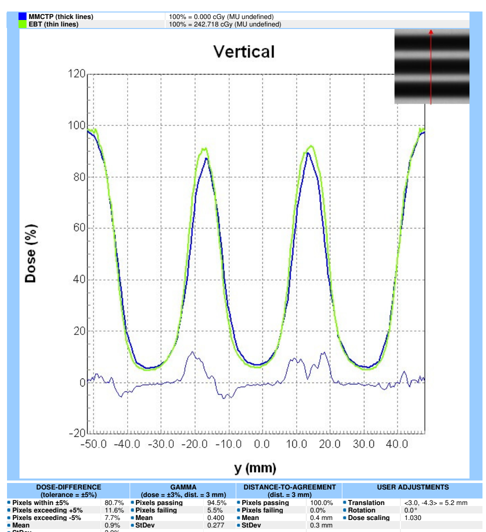

(c) Profile comparison between MC and film measurements for 6 MeV electrons in the bone phantom.

Figure 6–7: Comparison of MC calculation and film measurements for a 15×15 cm^2 6 MeV electron beam in the bone phantom.

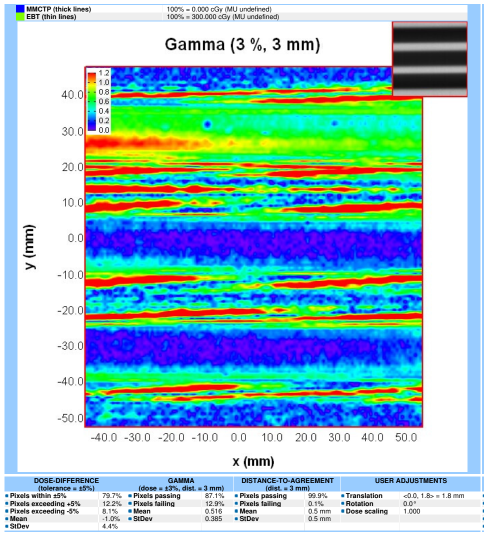

(a) Gamma comparison between MC calculations and film measurements for 9 MeV electrons in the bone phantom.

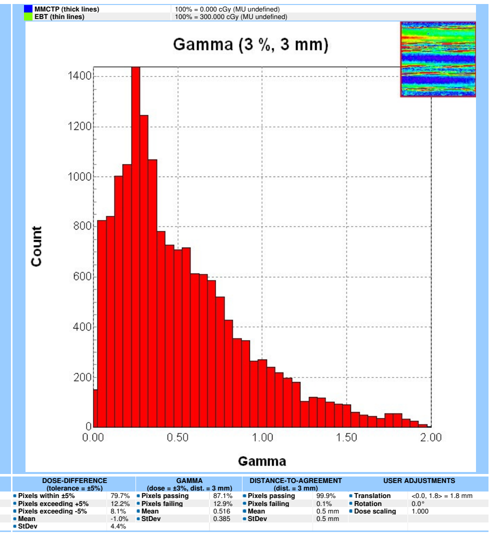

(b) Histogram of the gamma map in 6–8a.

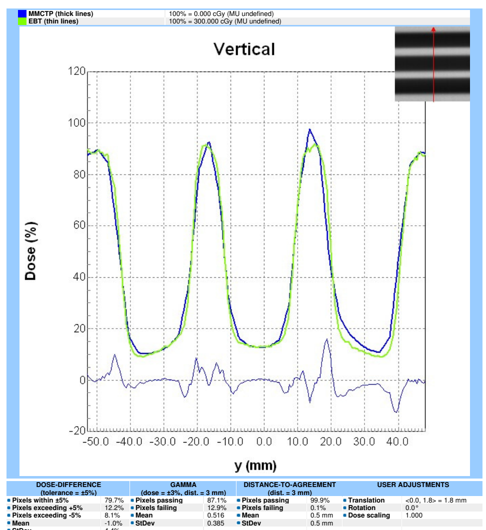

(c) Profile comparison between MC and film measurements for 9 MeV electrons in the bone phantom.

Figure 6–8: Comparison of MC calculation and film measurements for a 15×15 cm^2 9 MeV electron beam in the bone phantom.

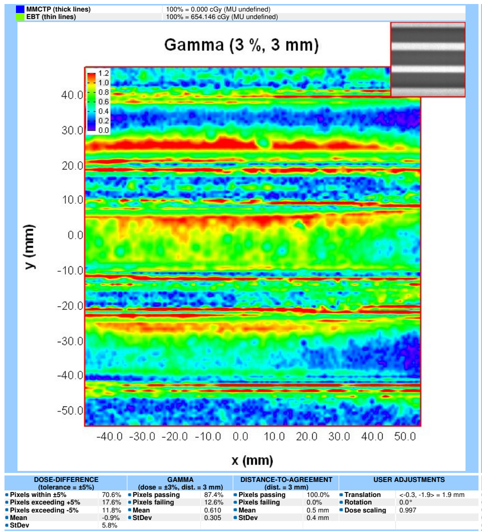

(a) Gamma comparison between MC calculations and film measurements for 12 MeV electrons in the bone phantom.

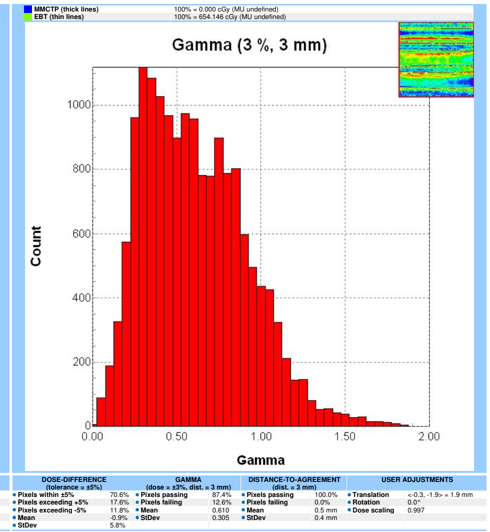

(b) Histogram of the gamma map in 6–9a.

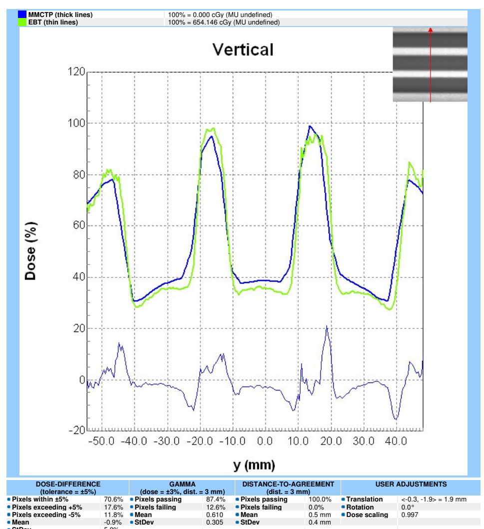

(c) Profile comparison between MC and film measurements for 12 MeV electrons in the bone phantom.

Figure 6–9: Comparison of MC calculation and film measurements for a 15×15 cm^2 12 MeV electron beam in the bone phantom.

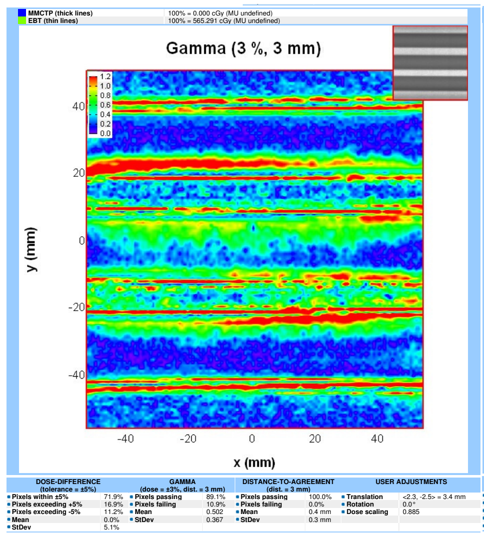

(a) Gamma comparison between MC calculations and film measurements for 16 MeV electrons in the bone phantom.

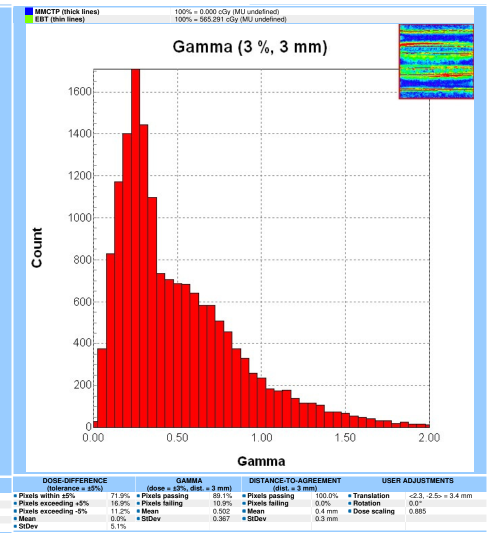

(b) Histogram of the gamma map in 6–10a.

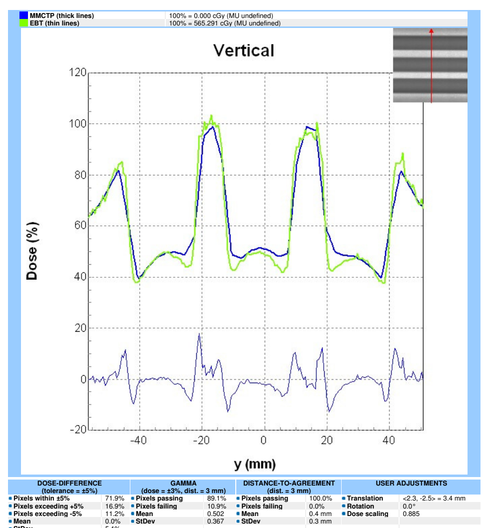

(c) Profile comparison between MC and film measurements for 16 MeV electrons in the bone phantom.

Figure 6–10: Comparison of MC calculation and film measurements for a 15×15 cm^2 16 MeV electron beam in the bone phantom.

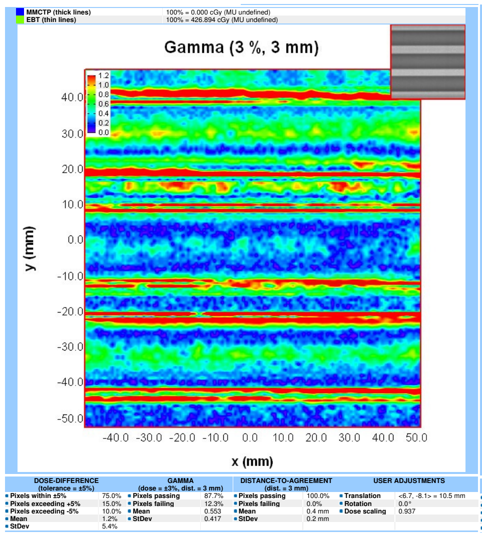

(a) Gamma comparison between MC calculations and film measurements for 20 MeV electrons in the bone phantom.

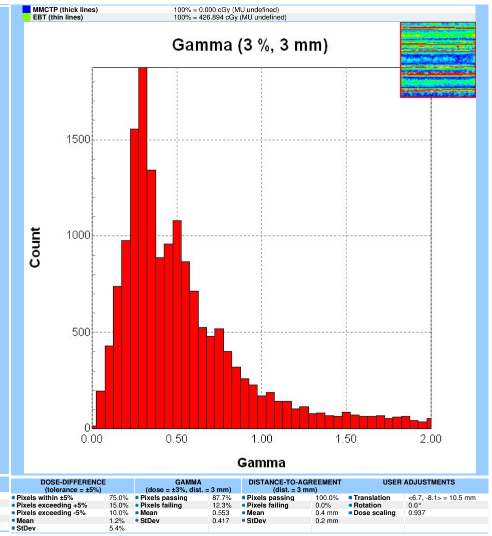

(b) Histogram of the gamma map in 6–11a.

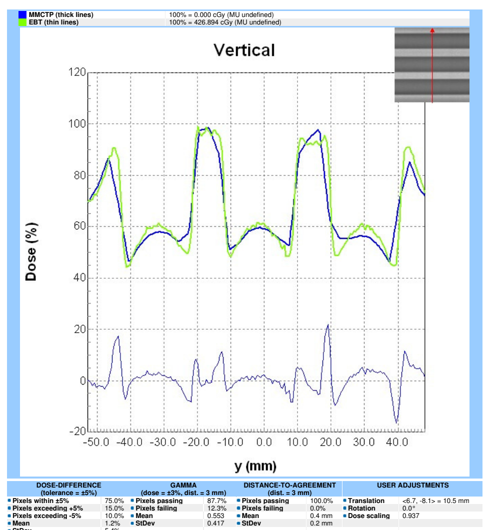

(c) Profile comparison between MC and film measurements for 20 MeV electrons in the bone phantom.

Figure 6–11: Comparison of MC calculation and film measurements for a 15×15 cm^2 20 MeV electron beam in the bone phantom.

The MC calculation system performed reasonably well for the bone phantom but not as well as for the lung phantom. Certain areas of the profile comparison show a difference of greater than 20% in the case of the 20 MeV beam (figure 6–11a), but it is worth noting, however, that the relatively large resolution of 3 mm of the MC calculated dose map is enhancing this discrepancy. The same criteria of 3% dose difference and 3 mm DTA was used in the gamma comparison. The percentage of pixels passing in the ROI for each energy is listed in table 6–2.

Energy (MeV)	Percentage of Pixels Passing
6	94.5%
9	87.1%
12	87.4%
16	89.1%
20	87.7%

Table 6–2: Percentage of pixels passing within the ROI used for the gamma comparison of the film measurements and MC calculated dose distribution in the bone phantom.

References

[1] G. Kamta. Evaluation of eclipse monte carlo dose calculation for clinical beams using heterogeneous phantoms. Master's thesis, McGill University, 2009.

CHAPTER 7
Conclusion and Future Work

Contents

7.1 Conclusions

The main objective of this work was to validate and render clinically implementable an electron beam MC treatment planning system. To do so, output factor calculation performance of the CUTOUT code had to be tested; 2D profiles in a Solid Water® phantom were measured and compared to MC calculated profiles; film measurements were acquired in two heterogenous phantoms and compared to simulated 2D dose maps.

The CUTOUT EGS user code enables us to digitize patient specific electron cutouts and propagates phase-space particles through it. This gives us the ability to calculate cutout output factors on a case by case basis and to determine 3D dose within patient. CUTOUT is incorporated into MMCTP so that when desired, the user can digitize a patient's cutout and submit the job all from within the MMCTP environment, thus making electron beam MC treatment planning relatively simple to perform.

Over forty electron cutout output factors were measured across different energies, applicator sizes and SSDs. The MC calculations were then performed using the Cutout Manager GUI where each output factor took approximately 2 hours to complete. The mean overall percentage difference between calculated and measured output factors was 1.31% with a mean error on each of the calculations of 1.56%. This low percentage difference between measured and calculated output factors means that using MC to calculate future output factors is a definite possibility. One advantage of calculating output factors over measuring them is that it will save a good deal of physicists' time in the clinic since they only need to digitize the cutout and let it calculate for 2 hours. Certain cutouts are too small relative to the energy used, this has the effect of shifting the location of maximum dose towards the surface, thus making the measurement more complicated since the true $z_{\max}$ must be determined. Using MC instead would take care of the shifted $z_{\max}$ for the physicist and could be used at the very least as a double-check since measuring output factors that are extremely low ($< 90\%$) can have a physicist second guess him/herself.

For the most part, the MC profile calculations in Solid Water® were in close agreement with the profile measurements in water. The two heterogenous phantoms gave a good opportunity to test the overall MC system within MMCTP. The CT of the phantom was converted into the EGSPHANT virtual phantom to test the viability of using the system for patient treatment planning. The results of the heterogeneous phantoms were acceptable with a high percentage of the pixels for each energy passing the gamma comparison with criteria of 3% dose difference and 3 mm distance-to-agreement.

7.2 Future Work

The clinical utilization of the MC output factor calculation is something we foresee happening, if at least for output factor verification. As it stands, we believe that the calculations can be trusted across all energies for applicator sizes of 6×6 cm^2, 10×10 cm^2 and 15×15 cm^2. It should be commissioned for 20×20 cm^2 as well for completeness. A Mac computer containing the CUTOUT user code and Cutout Manager GUI should be available within the JGH clinic for output factor calculations. The heterogenous performance should be further looked into and fine tuned but are still reasonable enough for patient recalculation if desired. Now that patient-specific cutouts can be calculated using MC, patient dose distributions can be retroactively calculated. A comparison between the MC framework discussed in this work with Varian's eMC module could also be investigated.

ABBREVIATIONS

ASCII	American Standard Code for Information Interchange
CM	Component module
CPU	Central processing unit
CSDA	Continuous slowing down appriximation
DC	Direct current
EGS	Electron Gamma Shower
GUI	Graphical user interface
Linac	Linear accelerator
MC	Monte Carlo
MeV	Megaelectron volt
MU	Monitor Unit
MV	Megavolt
NRC	Nuclear Research Council of Canada
PDD	Percent depth dose
PSF	Phase space file
ROI	Region of interest
TP	Treatment planning
voxel	Volume element

REFERENCES

[1] http://www.gammex.com/.

[2] A. Alexander, F. DeBlois, G. Stroian, K. Al-Yahya, E. Heath, and J. Seuntjens. Mmctp: a radiotherapy research environment for monte carlo and patient-specific treatment planning. *Physics in Medicine and Biology*, 2007.

[3] P.R. Almond, A.E. Wright, and M.L.M Boone. High energy electron dose perturbations in regions of tissue heterogeneity. *Radiol.*, 1967.

[4] P. Andreo. Monte carlo techniques in medical radiation physics. *Phys. Med. Biol.*, 36(7):861–920, 1991.

[5] F. Bagne. Electron beam treatment-planning system. *Med. Phys.*, 1976.

[6] J. Berger. Monte carclo calculation of the penetration and diffusion of fast charged particles. *Methods in Computational Physics*, 1963.

[7] C. Constantinou, F.H. Attix, and B.R. Paliwal. A solid water phantom material for radiotherapy x-ray and gamma-ray beam calibrations. *Med. Phys*, 1982.

[8] A. Dahler, A.S. Baker, and J.S. Laughlin. Comprehensive electron bea treatment planning. *Ann. N.Y. Acad. Sci*, 1969.

[9] Slobodan Devic, Jan Seuntjens, Edwin Sham, Ervin B. Podgorsak, C. Ross Schmidtlein, Assen S. Kirov, and Christopher G. Soares. Precise radiochromic film dosimetry using a flat-bed document scanner. *Medical Physics*, 32(7):2245–2253, 2005.

[10] I. J. Chetty et al. Report of the aapm task group no. 105: Issure associated with clinical implementation of monte carlo-based poton and electron external beam treatment planning. Technical report, AAPM, 2007.

[11] H.E. Johns and J.R. Cunningham. *The Physics of Radiology.* Thomas, fourth edition, 1983.

[12] G. Kamta. Evaluation of eclipse monte carlo dose calculation for clinical beams using heterogeneous phantoms. Master's thesis, McGill University, 2009.

[13] I. Kawrakow and D. W. O. Rogers. The egsnrc code system: Monte carlo simulation of electron and photon transport. Technical report, National Research Council of Canada, 2006.

[14] J.S. Laughlin. High energy electron treatment planning for inhomogeneities. *British Journal of Radiology*, 38(143), 1965.

[15] B. Markus. Energiebestimmung schneller elektronen aus tiefendosiskurben. *Strahlentherapie*, 1961.

[16] C.G. Orton and F. Bagne, editors. *Practical Aspects of Electron Beam Treatment Planning*. American Association of Physicists in Medicine, American Institute of Physics, 1978.

[17] E. B. Podgorsak, editor. *Radiation Oncology Physics: A Handbook for Teachers and Students*. International Atomic Energy Agency, Vienna, 2005.

[18] E. B. Podgorsak. *Radiation Physics for Medical Physicists*. Springer, first edition, 2006.

[19] D. W. O. Rogers. Fifty years of monte carlo simulations for medical physics. *Phys. Med. Biol.*, 51:287–301, 2006.

[20] D. W. O. Rogers, B. A. Faddegon, G. X. Ding, C.-M Ma, and J. We. Beam: A monte carlo code to simulate radiotherapy treatment units. *Med. Phys.*, 22(5):504–523, May 1995.

[21] D. W. O. Rogers, B. Walters, and I. Kawrakow. *BEAMnrc User's Manual*. NRC, 2009.

[22] H. Svensson and G. Hettinger. The influence of the collimating system on the dose distribution from 10 to 35 mev electron radiation. *Acta Radiologica*, 1967.

[23] J. Thébaut. Measurement driven, electron beam modeling and commissioning for a monte carlo treatment planning system with improved accuracy. Master's thesis, McGill University, 2009.

[24] B. Walters. *DOSXYZnrc Users Manual*. NRC, 2009.